

AnyCXR: Human Anatomy Segmentation of Chest X-ray at Any Acquisition Position using Multi-stage Domain Randomized Synthetic Data with Imperfect Annotations and Conditional Joint Annotation Regularization Learning

Zifei Dong^{a,b,1}, Wenjie Wu^{c,d,1}, Jinkui Hao^a, Tianqi Chen^a, Ziqiao Weng^{a,e}, Bo Zhou^{a,*}

^aDepartment of Radiology, Northwestern University, Chicago, IL, USA

^bData Science Institute, Vanderbilt University, Nashville, TN, USA

^cDepartment of Orthopedics, The Second Hospital of Shanxi Medical University, Taiyuan, Shanxi, P.R. China

^dSecond Clinical Medical College, Shanxi Medical University, Taiyuan, Shanxi, P.R. China

^eSchool of Computer Science, University of Sydney, Sydney, NSW, Australia

ARTICLE INFO

Article history:

Keywords: Chest X-ray, Segmentation, Synthetic Data, Imperfect Annotation, Domain Randomization

ABSTRACT

Robust anatomical segmentation of chest X-rays (CXRs) remains challenging due to the scarcity of comprehensive annotations and the substantial variability of real-world acquisition conditions. We propose AnyCXR, a unified framework that enables generalizable multi-organ segmentation across arbitrary CXR projection angles using only synthetic supervision. The method combines a Multi-stage Domain Randomization (MSDR) engine, which generates over 100,000 anatomically faithful and highly diverse synthetic radiographs from 3D CT volumes, with a Conditional Joint Annotation Regularization (CAR) learning strategy that leverages partial and imperfect labels by enforcing anatomical consistency in a latent space. Trained entirely on synthetic data, AnyCXR achieves strong zero-shot generalization on multiple real-world datasets, providing accurate delineation of 54 anatomical structures in PA, lateral, and oblique views. The resulting segmentation maps support downstream clinical tasks, including automated cardiothoracic ratio estimation, spine curvature assessment, and disease classification, where the incorporation of anatomical priors improves diagnostic performance. These results demonstrate that AnyCXR establishes a scalable and reliable foundation for anatomy-aware CXR analysis and offers a practical pathway toward reducing annotation burdens while improving robustness across diverse imaging conditions.

arXiv Preprint.

1. Introduction

Chest X-ray (CXR) is the most widely used medical imaging modality, with billions of examinations performed each year worldwide (Akhter et al., 2023). Its low cost, rapid acquisi-

tion, and minimal radiation exposure make it a cornerstone and first-line imaging technique across cardiothoracic, pulmonary, and musculoskeletal disease workflows, playing a pivotal role in the early screening of conditions such as pneumonia, tuberculosis, and lung cancer (Gaggion et al., 2024). In contrast to CXR, cross-sectional modalities such as Computed Tomography (CT) and Magnetic Resonance Imaging (MRI) benefit from well-defined three-dimensional anatomical boundaries and standardized acquisition geometries, enabling the development of highly reliable and widely adopted deep learning

*Corresponding author.

e-mail: zifei.dong@vanderbilt.edu (Zifei Dong),

bo.zhou@northwestern.edu (Bo Zhou)

¹These authors contributed equally to this work.

(DL)-based anatomical segmentation tools, such as CT TotalSegmentator (Wasserthal et al., 2023) and MRI TotalSegmentator (Akinçi D’Antonoli et al., 2025; Isensee et al., 2021). These tools have become integral to organ- and lesion-specific analysis in CT and MRI and are routinely used in both clinical research and downstream automated pipelines (Sebro and Mongan, 2023). However, despite the pervasive use of CXR in clinical practice, no generalizable or robust segmentation framework exists for CXRs that can delineate a comprehensive set of anatomical structures across diverse acquisition conditions. Creating such a model is a critical step toward automated anatomical reasoning and downstream clinical AI tasks on radiographs, yet it remains technically challenging due to the unique properties of CXR imaging (Hou et al., 2024).

Several fundamental obstacles hinder this progress. The most critical limitation is the lack of large-scale, consistently well-annotated CXR datasets. While prior efforts have targeted segmentation of specific anatomical regions such as the lungs, heart, or clavicles, most methods remain restricted to standard posteroanterior (PA) or anteroposterior (AP) views and depend heavily on time-consuming manual annotations (Calli et al., 2021; Yi et al., 2025). Historically, two major categories of solutions have been explored. The first comprises traditional computer vision frameworks that rely on mathematically defined heuristics and hand-crafted features (Xue and Niu, 2024). Approaches such as edge detection, active contour models, or statistical shape priors can capture local intensity transitions or shape regularities, yet they often require extensive parameter tuning and are highly sensitive to noise and acquisition variability (van Ginneken et al., 2006; Candemir and Antani, 2019). As a result, their performance quickly deteriorates when applied to heterogeneous, real-world clinical datasets. The second category, more recent and data-driven, employs DL-based architectures trained on human-annotated CXR datasets (Seibold et al., 2022). Although such models achieve higher accuracy and improved generalization compared to classical methods, they are fundamentally constrained by the inherent ambiguity and incompleteness of 2D manual annotations (Wang et al., 2024).

Label inconsistencies across institutions, annotators, and imaging systems introduce substantial inter-dataset domain shifts (Tajbakhsh et al., 2020). Moreover, CXR annotations reflect contrast-based visible boundaries rather than true anatomical surfaces (Lenga et al., 2019). For example, the delineated lung fields typically correspond to air-tissue contrast regions, while the actual lung anatomy extends posteriorly behind the heart and diaphragm (Sharma et al., 2024). Likewise, bony structures such as the spine are difficult to annotate precisely due to overlapping anatomy and projection ambiguity.

In clinical practice, CXR data are also remarkably heterogeneous. Even within standardized PA views, patient positioning, breathing state, and X-ray beam alignment vary considerably, producing differences in projection angle and field of view (Gothi, 2025). Additional variability arises from factors such as detector type, acquisition parameters, and patient habitus, all of which alter image appearance and contrast distribution. Consequently, models trained on fixed-view or narrow-domain datasets often fail when applied to oblique or other non-

standard projections (Jones et al., 2021). This stands in stark contrast to CT, where imaging geometry and attenuation properties are standardized and 3D annotation is anatomically consistent (Hofmann et al., 2025). The result is a persistent gap: while CT- and MRI-based segmentation tools are mature and generalizable, CXR segmentation remains fragile and domain-specific (Qin et al., 2018).

To mitigate these limitations on the real CXR data, recent studies have investigated generating synthetic X-rays from 3D CT volumes to provide anatomically consistent training data. By forward-projecting CT scans into 2D Digitally Reconstructed Radiographs (DRRs), researchers can generate realistic radiographs with pixel-perfect labels directly derived from 3D anatomical segmentations. For example, Gao et al. (2023) proposed the SyntheX framework, demonstrating that DL models trained exclusively on simple DRRs with image-based data augmentation can match or even outperform those trained on real pelvic X-ray data. Similarly, Seibold et al. (2023) applied a CT-to-DRR approach for chest imaging and observed high agreement between synthetic and real CXR predictions when evaluated against expert annotations.

These studies demonstrated the feasibility of using CT-derived DRRs to produce anatomically precise, scalable datasets for CXR segmentation. Nonetheless, existing synthetic frameworks remain limited in both scope and realism. First, most prior works generated relatively small datasets (i.e., often only hundreds to a few thousand images) using fixed projection parameters or simplistic post-hoc augmentations, which inadequately capture the diversity and variation encountered in real clinical acquisitions (Qureshi et al., 2023). Second, while automatic CT-based labeling tools such as TotalSegmentator (Wasserthal et al., 2023) facilitate large-scale label creation, their segmentation quality varies across anatomical structures, leading to incomplete or noisy ground truth prior to the projection. This introduces another unique challenge: *how can a network be trained effectively on large-scale synthetic data that are partially labeled, imperfectly annotated, and highly diverse?* Addressing this challenge requires innovations in both data generation and model learning paradigms.

In this work, we propose **AnyCXR**, a comprehensive framework for generalizable human anatomical segmentation on CXRs acquired at any acquisition angle. The proposed framework integrates two synergistic components. First, we introduce a **Multi-stage Domain Randomization (MSDR)** synthetic data generation pipeline that systematically projects 3D CTs into DRRs while applying staged random perturbations to anatomical structures, projection geometry, and intensity characteristics. By independently modulating contrast, appearance, and attenuation patterns of different tissue components across multiple randomization stages, the pipeline simulates a broad spectrum of projection angles, patient orientations, and image appearances. This enables the generation of over 100,000 diverse synthetic CXRs that more faithfully reflect the variability observed in real-world practice and out-of-distribution settings. To ensure annotation reliability, we further develop an automatic label-quality selection mechanism that performs multi-level sanity checks on each generated mask, thereby curating a

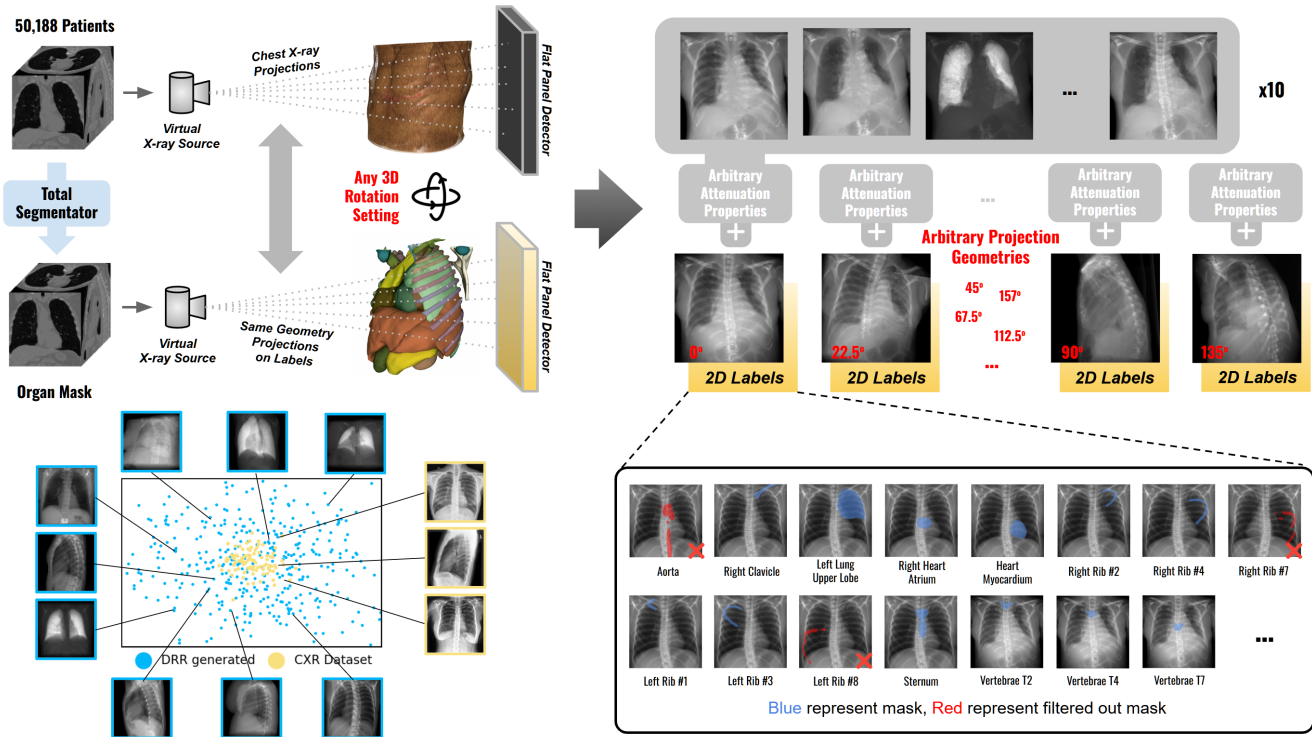


Figure 1: **AnyCXR Data Pipeline:** This workflow projects 3D CT volumes into diverse 2D Digitally Reconstructed Radiographs (DRRs) and segmentation masks using Multi-stage Domain Randomization. The pipeline includes an automated filtering step that discards invalid masks (red). The feature plot (bottom left) demonstrates that this method generates a data distribution significantly broader than typical real-world datasets.

dataset with verified, partial, yet reliable labels. Second, building on this curated dataset, we design the **Conditional Joint Annotation Regularization (CAR)** learning framework to enable effective training from incomplete supervision. CAR extends joint regularization learning to multi-anatomical segmentation by transferring features into a latent representation and imposing conditional consistency constraints across overlapping anatomical structures. This allows the model to leverage all available data (*i.e.*, both complete and partial annotations) while maintaining inter-organ coherence. Comprehensive experiments demonstrate that AnyCXR produces anatomically precise segmentation on both synthetic and real CXRs, improving robustness across unseen projection angles. Moreover, we show that the resulting anatomical maps enhance downstream clinical and AI tasks, such as cardiomegaly assessment, scoliosis measurement, and general CXR disease classification. Our contributions are summarized as follows:

- A Multi-stage Domain Randomization (MSDR) pipeline that generates large-scale, highly diverse, and high-fidelity synthetic CXRs across diverse projection geometries and appearance variations.
- A label-quality selection and filtering mechanism that ensures robust training with imperfect or partial CT-derived annotations.
- A novel Conditional Joint Annotation Regularization (CAR) framework enabling multi-anatomical segmentation from incomplete supervision.
- Extensive validation on both simulated and real-world

datasets, demonstrating AnyCXR’s generalization to arbitrary acquisition angles and its utility in multiple downstream clinical AI applications.

2. Methods

In this section, we provide an overview of the two core components of our framework and how they jointly enable robust CXR segmentation. First, we introduce the Multi-Stage Randomized Synthetic AnyCXR data-generation engine and the accompanying label quality-control pipeline, which together produce large, diverse datasets paired with high-quality partial organ annotations (Section 2.1). Second, using these partially annotated datasets, we present the Conditional Joint Annotation Regularization (CAR) learning framework, which leverages partial labels and a latent-space regularization strategy to train a unified segmentation model capable of delineating all anatomical structures while preserving anatomical context (Section 2.2). Implementation details for both components are summarized in Section 2.3, and the study design and evaluation strategies are detailed in Section 2.4.

2.1. AnyCXR Generation Engine

An overview of the AnyCXR generation engine is shown in Fig. 1. The engine converts volumetric chest CT scans into radiograph-like projections, producing anatomically faithful, label-aligned synthetic CXRs for large-scale model training. The pipeline consists of two components: (1) segmentation-driven data curation to ensure anatomical plausibility and label

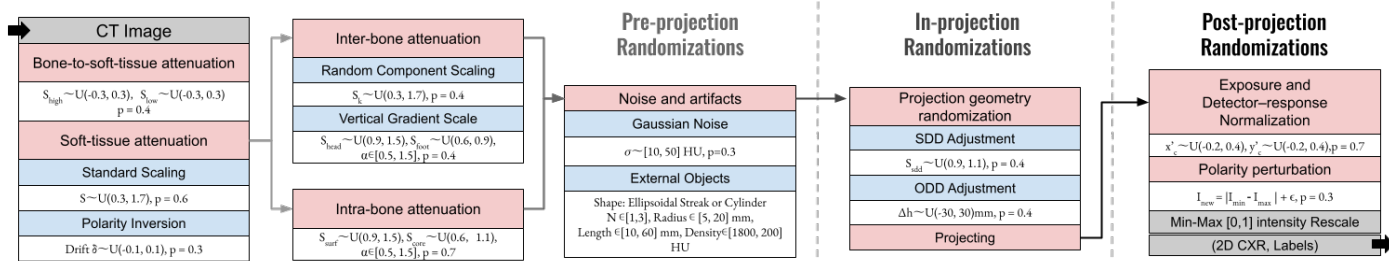


Figure 2: **MSDR Pipeline**: This flow chart details the Multi-stage Domain Randomization engine, which converts 3D CT data into 2D synthetic DRRs through a sequence of stochastic steps. The pipeline involves Pre-projection Randomizations acting on Hounsfield Units and image artifacts, In-projection Randomizations modifying geometry, and Post-projection Randomizations simulating detector response and inverting polarity. The red boxes denote randomization names, while blue boxes denote different approaches.

reliability, and (2) a multi-stage randomized projection process that produces diverse CXRs paired with the curated labels.

Anatomical Label Presence by % (2,982 Patients)

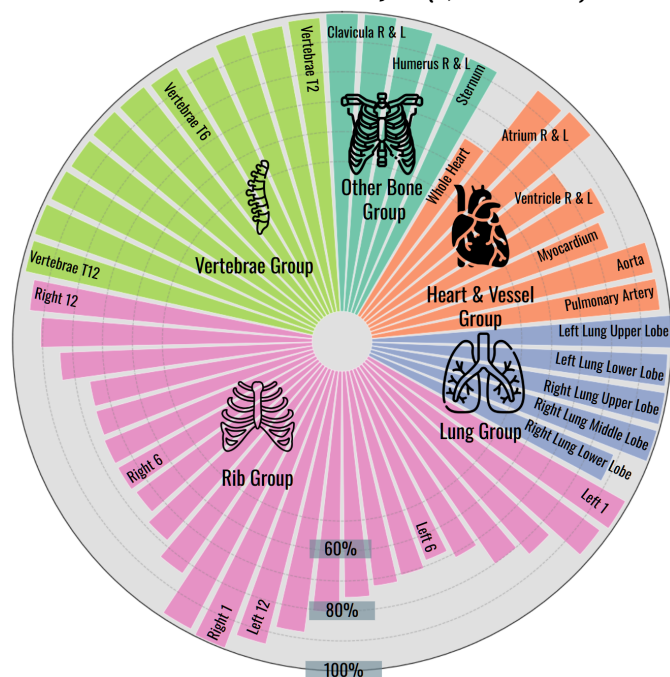


Figure 3: **Distribution of organ annotations after filtering**: This chart shows the anatomical label presence percentage across the 2,982 curated patient CT volumes after the two-stage quality control process. The distribution is grouped by major anatomical categories (Bone, Heart and Vessels, Lung, Rib, and Vertebrae), demonstrating the partial yet high-quality nature of the training dataset used for AnyCXR.

2.1.1. Data Curation and Quality Control

We begin by generating fine-grained anatomical masks for the CT-RATE dataset (Hamamci et al., 2024) (50,188 non-contrast chest CT scans from 21,304 patients) using CT TotalSegmentator (TS) (Wasserthal et al., 2023). Because the raw TS outputs exhibit variable reliability across this large and heterogeneous cohort, we introduce a two-stage segmentation-driven Quality Control (QC) procedure to ensure stable and trustworthy labels prior to projection.

Stage 1: 3D Anatomical Consistency Check. This stage assesses the structural plausibility and integrity of each 3D mask to filter out volumes with severe segmentation failures. We focus on major skeletal structures, particularly the thoracic vertebrae, which serve as a sentinel for overall mask fidelity. For each CT volume, adjacent vertebral elements along the superior–inferior axis are examined slice-wise. A volume is discarded if (i) neighboring components exhibit substantial overlap or (ii) an implausible number of distinct elements appear within a single axial slice (e.g., three vertebrae in one slice, which is anatomically impossible). This 3D consistency rule removes the majority of gross segmentation errors. Volumes passing this check (2,982 CT scans) are retained for further QC and assumed to have predominantly reliable anatomy labels.

Stage 2: Per-Class Mask Reliability Check in 2D Projections. The retained 3D masks are projected into DRRs at evenly spaced source–detector rotations from 0° to 180° . For each view, we evaluate per-class mask reliability via a two-step process. First, isolated small components are removed by discarding connected components below a minimal fraction of the class’s largest component. If a second large component remains after cleanup, the class is flagged as unreliable and excluded from supervision for all projections of that CT. After this refinement, we retain a taxonomy of 54 anatomical classes, including cardiac chambers, great vessels, lung lobes, ribs (1–12), thoracic vertebrae (T2–T12), sternum, clavicles, and proximal humeri. Together, these QC procedures yield a curated dataset of 2,982 CT scans with high-quality partial segmentation labels suitable for downstream AnyCXR generation. The distribution of each organ is visualized in Fig. 3 and the detailed numbers are in **Appendix C**.

2.1.2. Multi-stage Domain Randomization (MSDR)

Standard DRR-based synthesis typically relies on 2D post-hoc augmentations (e.g., noise, brightness shifts). However, such operations do not capture the inherently 3D physical factors that drive appearance variation in real CXRs and beyond, such as bone-to-soft-tissue contrast under different exposures, heterogeneous bone mineralization, and complex tissue overlap.

To overcome these limitations, we propose Multi-stage Domain Randomization (MSDR). The workflow is illustrated in

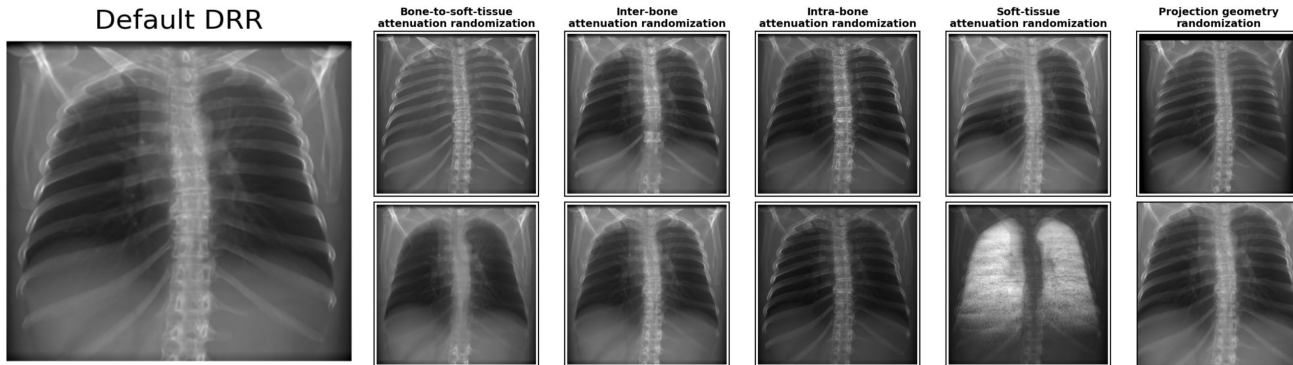


Figure 4: **DRR Augmentation Demonstration for Major Innovation:** This figure visually illustrates the effect of the primary Multi-stage randomization on the resulting DRR, starting from a Default DRR (left panel). Each subsequent column shows a different major 3D randomization applied in isolation: Bone-to-soft-tissue, Inter-bone, Intra-bone, Soft-tissue, and Projection geometry randomization, demonstrating how these 3D perturbations introduce diverse image appearances and contrast variations.

Fig. 2 with technical details summarized in **Appendix A**, inspired by Representation Learning (Dey et al., 2024) and AnyStar (Dey et al., 2023). Our MS DR engine performs the first stage of randomization directly in 3D *before* projection. This “pre-projection” strategy perturbs the *causes* of radiographic variability, producing a richer and more realistic distribution of DRRs. We introduce four principal 3D augmentation modules to modulate Hounsfield Units (HU), simulate structural variability, and alter projection behavior:

- **Bone-to-soft-tissue attenuation randomization:** To replicate variations in bone–soft-tissue contrast arising from different exposure settings, we apply anti-correlated scaling factors to bone and soft tissue. Intensities are sampled from complementary intervals to disrupt consistent contrast relationships (e.g., attenuating bone signals while amplifying soft tissue).
- **Inter-bone attenuation randomization:** To enhance bone density heterogeneity, we independently perturb the attenuation of individual osseous components (e.g., vertebrae, ribs) to decouple adjacent structures, or introduce longitudinal intensity gradients to simulate varying anatomical thickness along the superior-inferior axis.
- **Intra-bone attenuation randomization:** To introduce realistic non-uniform bone density, we apply a morphology-based gradient that modulates attenuation as a function of voxel depth. This simulates the natural transition from the dense cortical surface to the trabecular core, creating heterogeneous internal textures.
- **Soft-tissue attenuation randomization:** To prevent the model from over-relying on absolute brightness for segmentation, we apply random multiplicative HU scaling perturbations to soft-tissue regions. Additionally, we introduce polarity inversion to simulate extreme contrast reversals, thereby generating a wider range of appearance variations.
- **Projection geometry randomization:** Source-to-Detector Distance (SDD) and Object-to-Detector Distance (ODD) are determined using available metadata when

present. Otherwise, we use dataset-average values from CT-RATE and apply small random drifts to simulate variability in clinical setup.

- **Noise and artifacts:** Gaussian noise is injected, and implant synthetic high-density objects (such as wires) are implanted to approximate common imperfections observed in clinical radiographs.

Following 3D augmentation, DRR projection is performed at a resolution of 512×512 using the modified CT intensities, and masks are propagated to all sampled view angles. After projection, in the second stage of 2D Detector-Level Randomization, we simulate detector physics and display characteristics using several 2D transformations:

- **Exposure and Detector–response Normalization:** A randomized piecewise-linear window/level mapping is applied to reduce variations arising from exposure settings and display tone curves.
- **Polarity perturbation:** With low probability, image polarity is inverted (followed by re-normalization) to discourage reliance on absolute intensity polarity.

Together, these pre-projection and post-projection randomizations form the MS DR engine, producing a highly diverse, physically plausible, and label-aligned synthetic CXR dataset for large-scale segmentation training. For a visual overview of the workflow logic and detailed implementation methods, please refer to Fig. 2 and **Appendix A**. We visualize the innovative 3D augmentation effect in Fig. 4.

2.2. Conditional Joint Annotation Regularization Model

The overall architecture is illustrated in Fig. 5. Specifically, our segmentation model is built on a U-Net (Ronneberger et al., 2015) backbone with a ResNet50 encoder (He et al., 2016) pre-trained on ImageNet (Deng et al., 2009). Given an input image \mathbf{X} , the network f_ϕ outputs probabilistic segmentation maps $\hat{\mathbf{Y}} = f_\phi(\mathbf{X})$.

To handle partially labeled data, the segmentation loss \mathcal{L}_{Seg} is computed selectively using a binary availability mask \mathbf{M} . Let

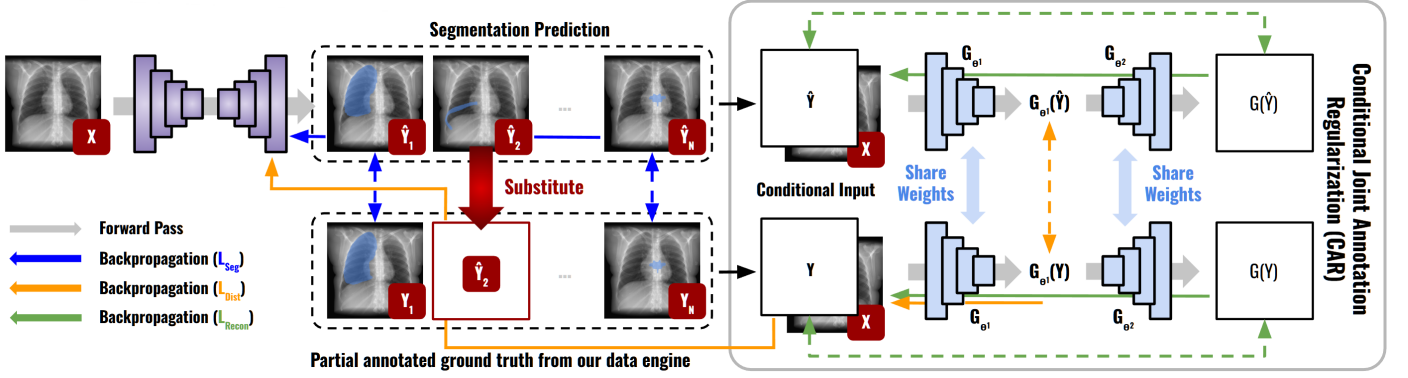


Figure 5: **CAR Framework Overview:** Input X-rays are segmented by a U-Net, with predictions substituting missing ground truth labels. Conditioned on image \mathbf{X} , these maps are encoded by G_{θ_1} to align their latent distributions via $\mathcal{L}_{\text{Dist}}$ (optimizing the U-Net), while the decoder G_{θ_2} ensures latent integrity via the reconstruction loss $\mathcal{L}_{\text{Recon}}$.

b denote the sample index within a batch of size B , and c denote the class index. The entry $\mathbf{M}^{(b,c)}$ is set to 1 if annotations exist for class c in sample b , and 0 otherwise. The loss is averaged over the available annotations:

$$\mathcal{L}_{\text{Seg}} = \frac{1}{\sum \mathbf{M}} \sum_{b,c} \mathbf{M}^{(b,c)} \cdot \mathcal{L}_{\text{Dice}}(\hat{\mathbf{Y}}^{(b,c)}, \mathbf{Y}_{gt}^{(b,c)}) \quad (1)$$

While simple, this strategy fails to leverage anatomical relationships between organs.

To leverage cross-organ context even under partial labels, we introduce a conditional autoencoding module, termed *Conditional Joint Annotation Regularization* (CAR). CAR enforces consistency between the predicted and anatomically plausible organ configurations, conditioned on the input image \mathbf{X} . CAR operates as an auxiliary autoencoder $G = G_{\theta_2} \circ G_{\theta_1}$ attached to the main segmentation head. Specifically, G_{θ_1} is the encoder that compresses the probability maps into a latent representation \mathbf{z} , which is used by the Distribution Loss ($\mathcal{L}_{\text{Dist}}$). G_{θ_2} is the decoder that reconstructs the maps from \mathbf{z} for the Reconstruction Loss ($\mathcal{L}_{\text{Recon}}$). The CAR framework operates on the main network’s probability maps and is driven by two key components:

Distribution Loss ($\mathcal{L}_{\text{Dist}}$): First, we construct a “reliable target” tensor, \mathbf{Y} . This composite tensor leverages the binary mask \mathbf{M} : where a valid ground truth \mathbf{Y}_{gt} exists, \mathbf{Y} uses \mathbf{Y}_{gt} ; otherwise, it uses the network’s prediction $\hat{\mathbf{Y}}$ with its gradients detached. This creates a complete pseudo-labeled target. Second, we apply conditional latent space regularization. The autoencoder compresses the prediction $\hat{\mathbf{Y}}$ and the target \mathbf{Y} into compact latent representations, $\mathbf{z}_{\hat{\mathbf{Y}}}$ and $\mathbf{z}_{\mathbf{Y}}$, via the encoder G_{θ_1} . To ensure conditioning on \mathbf{X} , we use a concatenation approach for all latent encodings where $\mathbf{z} = G_{\theta_1}(\text{Concat}(\mathbf{X}, \mathbf{Y}))$. This latent space is regularized by the Distribution Loss ($\mathcal{L}_{\text{Dist}}$), which is the core of CAR, minimizing the cosine distance between the latent representations of the prediction and the target:

$$\mathcal{L}_{\text{Dist}} = \frac{1}{B} \sum_{b=1}^B \left(1 - \frac{\mathbf{z}_{\hat{\mathbf{Y}}}^{(b)} \cdot \mathbf{z}_{\mathbf{Y}}^{(b)}}{\|\mathbf{z}_{\hat{\mathbf{Y}}}^{(b)}\| \|\mathbf{z}_{\mathbf{Y}}^{(b)}\|} \right) \quad (2)$$

Minimizing this distance forces the model’s output $\hat{\mathbf{Y}}$ to in-

hibit a latent structure that is consistent with anatomically correct organ layouts, effectively teaching it a shared anatomical prior. When the model is uncertain about an unlabeled organ, this loss encourages it to produce a prediction that is anatomically plausible given the input image \mathbf{X} and the other, correctly-predicted organs.

Reconstruction Loss ($\mathcal{L}_{\text{Recon}}$): To ensure that the encoder G_{θ_1} learns a meaningful, non-trivial compression (rather than a trivial solution), the decoder G_{θ_2} attempts to reconstruct the full probability maps from their latent representations. We use a Mean Squared Error (MSE) loss, as the autoencoder inputs are continuous probability maps. The reconstruction targets are detached to prevent the model from learning a trivial identity function:

$$\mathcal{L}_{\text{Recon}} = \mathcal{L}_{\text{MSE}}(G_{\theta_2}(\mathbf{z}_{\hat{\mathbf{Y}}}), \hat{\mathbf{Y}}_{\text{detach}}) + \mathcal{L}_{\text{MSE}}(G_{\theta_2}(\mathbf{z}_{\mathbf{Y}}), \mathbf{Y}_{\text{detach}}) \quad (3)$$

The final objective function combines the segmentation loss with the weighted CAR losses:

$$\mathcal{L}_{\text{Total}} = \mathcal{L}_{\text{Seg}} + \lambda_{\text{Dist}} \mathcal{L}_{\text{Dist}} + \lambda_{\text{Recon}} \mathcal{L}_{\text{Recon}} \quad (4)$$

where λ_{Dist} and λ_{Recon} are balancing hyperparameters. By integrating this module, the model learns powerful contextual rules, using information from labeled organs to infer the probable location and shape of unlabeled ones.

2.3. Implementation details

Synthetic projection and Multi-stage randomization: We use DiffDRR (Gopalakrishnan and Golland, 2023) and the projection geometry follows CT-RATE metadata when available; otherwise we adopt SDD as 1183 mm and ODD as 167 mm with a $\pm 10\%$ drift. The patient–detector translation is applied along the detector axis as $\Delta = \text{SDD} - \text{ODD}$. Volumes are resampled to the native spacings specified in the metadata, clipped to $[-1000, 2000]$ HU, and normalized following CT-RATE practice. We render nine view angles from 0° to 180° in 22.5° steps, covering the standard Anteroposterior (AP), Posteroanterior (PA), and Lateral (LA) views, and including multiple Oblique (OB) projections. After rendering, images are min–max normalized to the $[0, 255]$ range and cast to uint8 format.

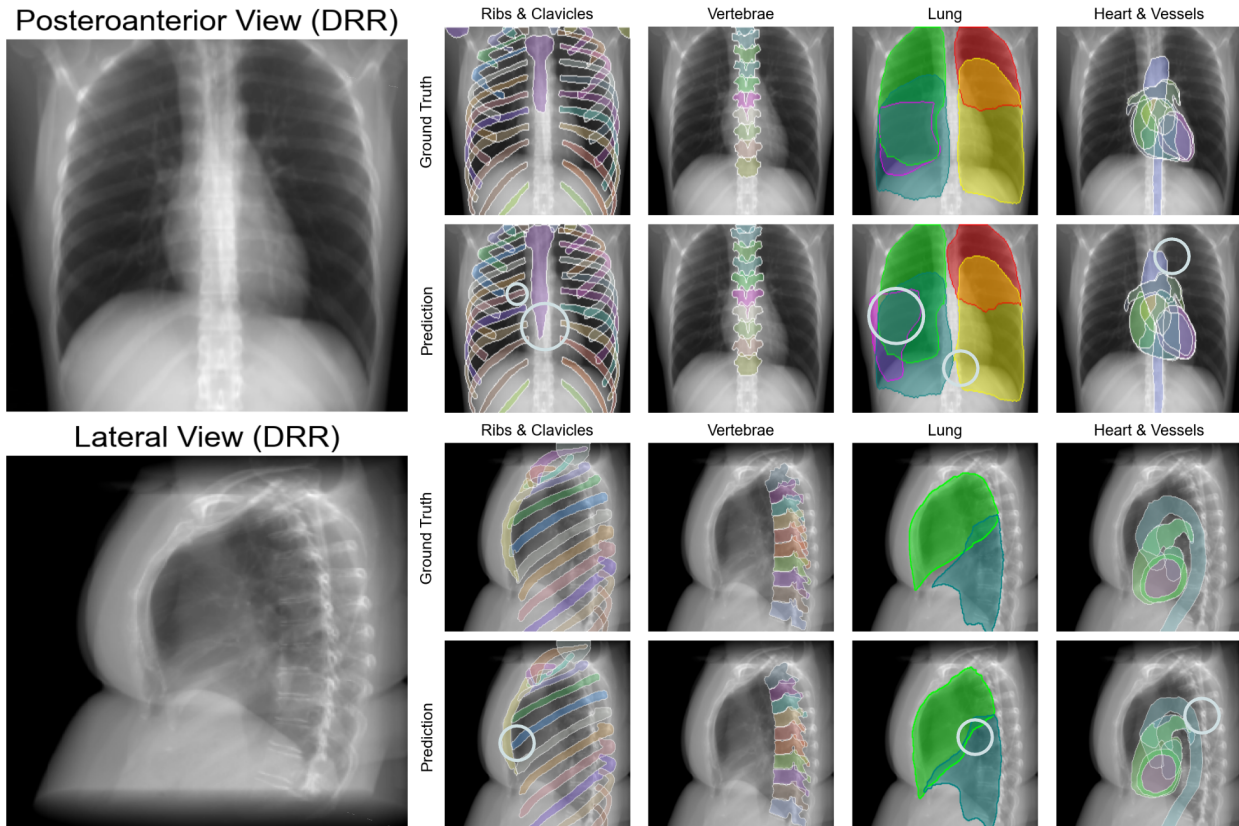


Figure 6: **Segmentation Comparison on Synthetic DRR:** This figure presents a side-by-side comparison of ground truth and model Prediction for major anatomical groups on the TotalSegmentator dataset. White circles indicate specific regions where the prediction deviated from the ground truth. While overall organ localization is highly accurate, the primary challenge is focused on subtle boundary adherence and fine detail resolution. The segmentation errors, particularly the fine organ boundaries of lungs and hearts, stem from the inherent difficulty in precisely delineating edges in the 2D projection plane, where overlap is severe and the model must rely heavily on learned anatomical priors to infer invisible or faint structures.

To expand the variability of DRR without breaking anatomy-mask alignment, we apply Multi-stage augmentation on the 3D volumes prior to projection (attenuation statistics, low-frequency bias, mild readout-like noise, sparse artifacts) and on the 2D image after projection (exposure normalization, rare polarity perturbation). Randomizations are applied deterministically with respect to each image-mask pair so that partial labels remain co-registered across all views.

We use a concise set of parameter ranges and probabilities that prove effective and stable in ablations; quantities not listed are sampled within narrow, non-critical defaults. Structure-wise HU drift is grouped by anatomy family (cardiac, great vessels, lungs, ribs, vertebrae, shoulder girdle) but sampled from the same range across groups.

All randomization modules preserve strict mask alignment and are compatible with partial-label supervision. This dataset consists of 2,982 CT scans with 126,410 variations in different views, along with their corresponding annotations.

CAR Training and Implementation Details: The segmentation backbone, a U-Net with an ImageNet-pretrained ResNet-50 encoder, was adapted by modifying its first convolutional block (conv1) to accept the single-channel CXR inputs, which

were preprocessed and normalized to the range $[0, 1]$. Optimization is performed using the Adam algorithm (Kingma and Ba, 2015) with an effective batch size of 24 (via $4\times$ gradient accumulation) and a staged learning rate decay schedule, starting at 1×10^{-4} and halved after rounds of 50, 80, and 128 epochs, while stability is maintained through mixed precision and gradient clipping (global norm of 1.0). After an initial 200-epoch warm-up, the CAR regularization module, with balancing hyperparameters set to $\lambda_{\text{Dist}} = 4$ and $\lambda_{\text{Recon}} = 2$, is trained for a further 200 epochs, and the entire training process utilizes five-fold cross-validation with a fixed random seed of 42 for reproducibility. The detailed model implementation is in **Appendix B**. All experiments were performed on Ubuntu 24.04.1 with an Intel i9-14900K, 64 GB RAM, and a single NVIDIA GeForce RTX 4090. DRRs are cached in host memory to accelerate batched processing.

2.4. Study Data Design and Evaluation Strategies

Segmentation Accuracy: We first quantify the segmentation fidelity of the 113 chest cases from the TotalSegmentator (TS) dataset (Wasserthal et al., 2023), which is curated with high-precision human annotations as a challenging zero-shot evaluation test set. For each test volume, DRRs are generated at

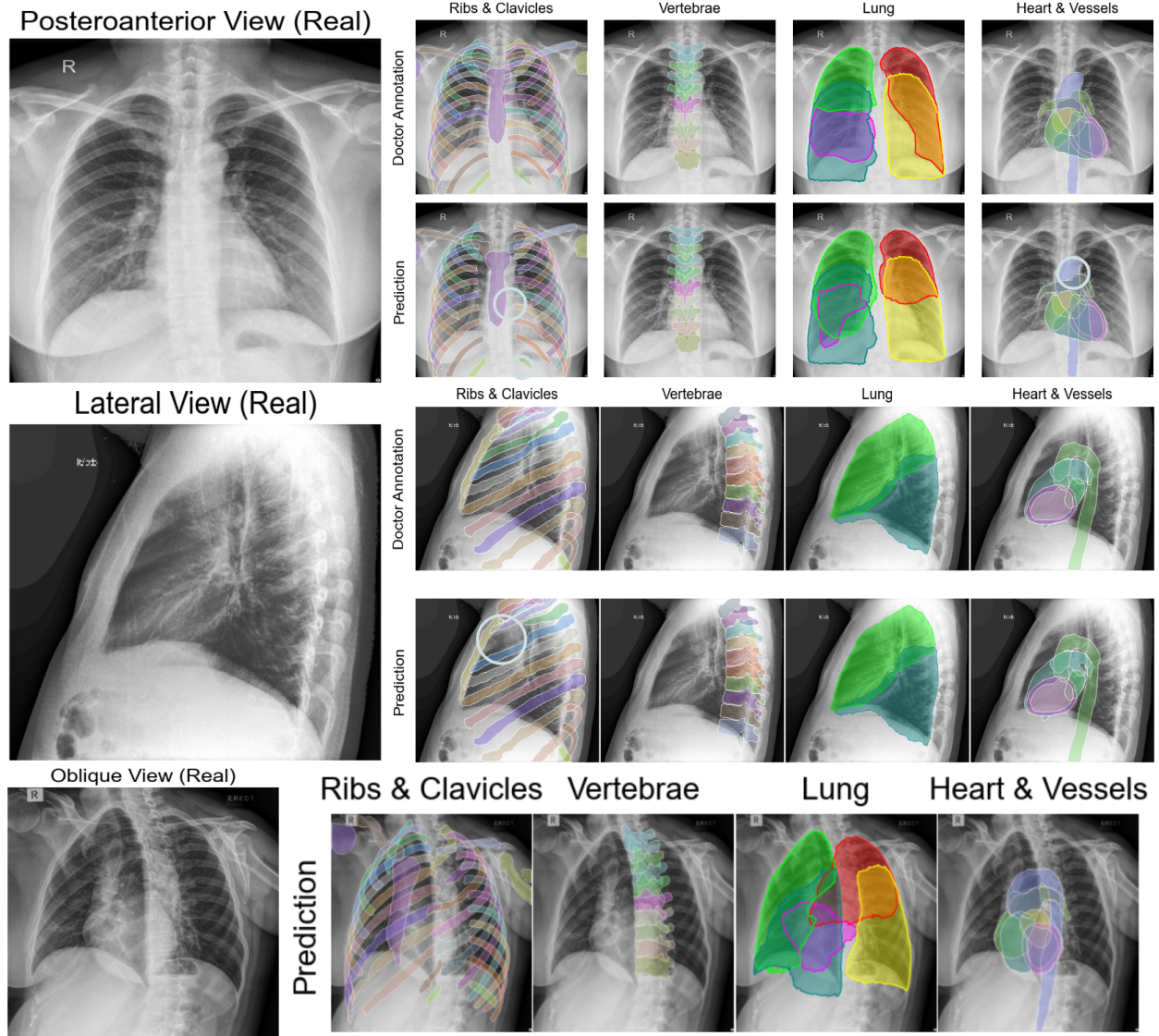


Figure 7: **Detailed Comparison of Segmentation on Real-World CXRs and Expert Refinement:** This figure presents a comparison of the model’s prediction against the expert corrections on real PA and LA view radiographs, highlighting the model’s generalization capability. White circles indicate specific regions where the prediction deviated from the expert annotation. While AnyCXR provides a highly effective initial segmentation proposal, these differences reflect areas of necessary expert editing. Specific challenges arise from image contrast variations and overexposure in clinical data, making detailed editing difficult, particularly for fine structures like the ribs and lungs. Furthermore, a non-trivial portion of the divergence relates to the inherent clinical ambiguity of 2D projection, such as precise lung lobe placement and boundary definition in superimposed regions, where the expert’s final delineation corrects the prediction based on clinical consensus.

the same discrete projection angles used during training. The primary metric is the Dice similarity coefficient (DSC), used in conjunction with the Hausdorff Distance (HD) to quantify spatial discrepancies; both metrics are computed per-class and macro-averaged across all 54 anatomical categories.

To assess real-world generalization, we randomly selected an external test set of PA and LA view radiographs from the ChestX-ray14 (CXR14) dataset (Wang et al., 2017), CheXpert (CXP) dataset (Irvin et al., 2019), MIMIC-CXR (MIMIC) dataset (Johnson et al., 2019), and Shenzhen Tuberculosis Chest X-rays (SZ) dataset (Jaeger et al., 2014). Specifically, we use the 10 SZ and 10 CXR14 samples for PA segmentation evaluation and the 10 CXP and 10 MIMIC samples for LA seg-

mentation evaluation. We enlisted an experienced chest physician to refine the model-generated segmentations within this 40-sample real-world test set, tasking them with correcting inaccuracies to the fullest extent possible to ensure the segmentations align with clinical gold standards. We report DSC and HD performance on this human-annotated benchmark, using the same metrics as the synthetic evaluation.

Downstream Clinical Applications: To evaluate the functional value of the learned anatomy, we integrate the predicted masks into three downstream tasks that model clinical workflows, especially in an initial physical examination. These tasks serve as end-to-end validations that the masks are not only geometrically accurate but also informative for preliminary diag-

nosis and quantification.

(1) *Cardiothoracic Ratio (CTR)*: We use the heart and lung masks from PA views to automatically derive the CTR. This is achieved by estimating the maximum cardiac and internal thoracic widths and computing the conventional (MRD+MLD)/ID ratio (Gupte et al., 2021). The evaluation for this task uses 1,593 positive cases and 1,593 negative cases from the CXR14 dataset and validates the stability of predicted masks for supporting basic, size-based quantification.

(2) *Thoracic Spine Curvature Assessment (SPCA)*: Leveraging instance-level vertebral segmentations (T2–T12), we compute a measure of thoracic spine deviation by assessing the average displacement of vertebral centroids from a fitted centerline (Maeda et al., 2023). This task is designed to provide a preliminary assessment of spinal curvature, stratifying cases into levels of severity to identify those that may require further evaluation or immediate attention. This task is evaluated on an in-house dataset with 12 positive cases provided by Shanxi Medical University and 2601 positive and 2601 negative cases from the MIMIC dataset. We clinically validated this methodology with a scoliosis expert, who confirmed its alignment with physical examination principles for identifying significant curvature.

(3) *Disease Classification with Segmentation-Guided Inputs*: To evaluate the diagnostic utility of anatomical guidance, we compare a disease classifier’s performance under two conditions using the full CXR14 dataset, which comprises 112,120 X-ray images with disease labels from 30,805 unique patients. We measured the Area Under the ROC Curve (AUC) (Hanley and McNeil, 1982) for all diseases, comparing a model trained on raw CXRs against one trained on a multi-channel input that includes the CXR image along with the predicted lung, bone, and heart masks (Azimi et al., 2022).

3. Experimental Results

In this section, we present a detailed analysis of our framework’s performance, structured to evaluate its core components and clinical utility. First, we quantify the segmentation accuracy and generalization of the model on both synthetic and real-world benchmarks (Section 3.1). Second, we conduct ablation studies to isolate and validate the contributions of the AnyCXR generation engine and the CAR framework (Section 3.2). Finally, we demonstrate the functional value of the learned anatomy through three distinct downstream clinical applications (Section 3.3).

3.1. Segmentation Accuracy and Generalization

We first evaluate the segmentation performance of the proposed AnyCXR-CAR model. We report the DSC and HD across all 54 anatomical classes on the zero-shot TS test set in Table 1, while the corresponding metrics for the oblique view are provided in detail in **Appendix E**. Performance is broken down by PA and LA views to demonstrate robust prediction across geometric variations. Specifically, the model achieved a mean DSC of 92.5% and an HD of 10.71 pixels in the PA view, while maintaining strong performance in the challenging LA view with a DSC of 88.8% and an HD of 20.41 pixels.

Overall, the framework demonstrates good performance across all of the major organ groups, as shown in Fig. 6, but it is not perfect, as boundary adherence remains a significant challenge, especially for regions with low contrast or severe superposition. Similar boundary ambiguity issues are reflected in the oblique view DRR segmentation in **Appendix D**. This issue is particularly notable at the boundaries of the Lung Group (DSC of around 95% in LA view), where the segmentation boundary derived from 3D CT projection is physically more accurate but inherently more complex than traditional human-drawn 2D annotations, leading to a higher expectation of error. This boundary ambiguity similarly affects the delineation of the Sternum, individual Ribs, and the middle of the spine (Vertebrae T4–T8, DSCs around 94% in PA view). It is also critical to note that the performance on the lower ribs (e.g., Rib Left 12, DSC 90.1% PA view) is not consistent because the lower ribs are often partially or entirely excluded from the original 3D CT training volumes, leading to model degradation due to a lack of complete training data.

To validate clinical readiness, we measure the macro-averaged DSC on the human-annotated real-world benchmark as shown in Table 2 complemented by Fig. 7. Specifically, the model demonstrated high fidelity in the PA view with a DSC of 97.8% for the Bone group, while achieving exceptional performance in the LA view for soft tissues, highlighted by DSCs of 98.2% for the Lung group and 96.7% for the Heart and Vessels.

3.2. Ablation Studies and Component Analysis

To isolate the contributions of our key innovations, we perform ablation studies, primarily focusing on the impact on macro-averaged DSC in the held out test set.

Contribution of CAR Regularization and MSDR: In our ablation analysis, we investigate the contribution of both the data augmentation strategy and the proposed CAR method. The five configurations studied are referred to by the following shorthand notation throughout the results section and figures: **Plain** refers to the baseline UNet architecture trained without any data augmentation; **PostHoc** denotes the UNet model trained exclusively using post-processing augmentation techniques; **MSDR** (or Non-Posthoc Augmentation) represents the UNet model trained solely with data after MSDR method; **Full Aug** represents the UNet model trained with the combined set of all augmentation techniques; and finally, **CAR + Aug** represents our full proposed architecture, which integrates the CAR model into the UNet framework and is trained with the optimal **Full Aug** strategy.

The progressive DSC gains detailed in Table 3 validate the effectiveness of our comprehensive data strategy, and the parallel HD improvements can be found in **Appendix F**. In the PA view, the MSDR configuration achieved a DSC of 94.03%, surpassing the PostHoc baseline of 93.75%, confirming the benefit of volumetric randomization. For the more challenging Lateral (LA) view, the synergy of both strategies proved critical: the Full Aug configuration achieved a DSC of 91.35%, significantly outperforming the Plain baseline of 85.98% and the PostHoc model at 89.16%.

The final integration of the CAR framework delivers the definitive performance gain, as visually confirmed in Fig. 8.

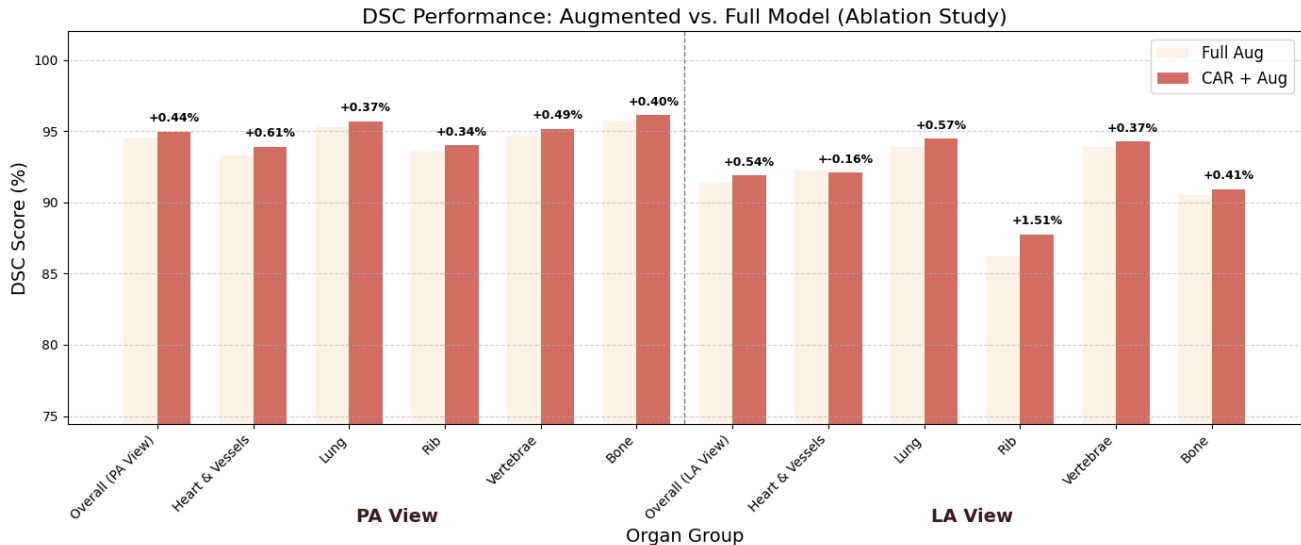


Figure 8: **Ablation Study of the CAR model:** This chart compares the DSC performance of the Full Aug model (MSDR + PostHoc augmentations) against the final CAR + Aug framework. The CAR framework consistently improves performance across all groups, with the largest gain (+1.51%) seen in the challenging Lateral Ribs group, validating CAR’s efficacy in enforcing anatomical priors where augmentation alone is insufficient.

Table 1: Zero-shot Performance (Dice and Hausdorff Distance) by Anatomical Structure for PA/LA Views on the TotalSegmentator Dataset

Structure	PA DSC↑	PA HD↓	LA DSC↑	LA HD↓	Structure	PA DSC↑	PA HD↓	LA DSC↑	LA HD↓
Vertebra T2	0.923	6.0	0.905	8.1	Whole Heart	0.929	19.3	0.935	15.9
Vertebra T3	0.935	5.6	0.919	6.8	Heart Atrium Left	0.905	10.4	0.888	10.6
Vertebra T4	0.930	7.7	0.907	9.9	Heart Atrium Right	0.920	10.1	0.894	15.3
Vertebra T5	0.928	8.1	0.923	11.5	Heart Myocardium	0.940	7.5	0.923	27.3
Vertebra T6	0.918	8.3	0.918	9.7	Heart Ventricle Left	0.936	7.6	0.868	54.1
Vertebra T7	0.920	8.5	0.924	7.2	Heart Ventricle Right	0.905	12.7	0.910	40.0
Vertebra T8	0.922	7.0	0.924	6.3	Pulmonary Artery	0.901	10.5	0.899	10.5
Vertebra T9	0.927	6.4	0.942	5.9	Aorta	0.914	16.8	0.896	20.5
Vertebra T10	0.938	7.5	0.932	5.5	Lung	0.930	23.86	0.916	30.92
Vertebra T11	0.944	7.6	0.929	8.3	Lung Upper Lobe Left	0.950	22.3	0.944	22.1
Vertebra T12	0.943	7.0	0.934	6.5	Lung Lower Lobe Left	0.944	23.9	0.934	26.1
Clavicle Left	0.946	5.2	0.914	18.2	Lung Upper Lobe Right	0.941	24.0	0.921	38.6
Clavicle Right	0.936	7.0	0.922	7.6	Lung Middle Lobe Right	0.872	27.5	0.853	38.5
Humerus Left	0.951	3.5	0.841	11.4	Lung Lower Lobe Right	0.943	21.6	0.928	29.3
Humerus Right	0.949	3.6	0.847	11.7	Sternum	0.918	17.1	0.923	26.9
Rib Left 1	0.933	7.8	0.854	10.6	Rib Right 1	0.938	6.7	0.884	8.4
Rib Left 2	0.898	18.1	0.866	7.0	Rib Right 2	0.906	11.4	0.861	9.2
Rib Left 3	0.921	8.9	0.897	6.6	Rib Right 3	0.910	10.1	0.877	7.5
Rib Left 4	0.925	11.0	0.891	10.7	Rib Right 4	0.910	11.8	0.886	18.2
Rib Left 5	0.918	10.4	0.876	10.1	Rib Right 5	0.921	11.2	0.856	18.5
Rib Left 6	0.924	9.9	0.850	21.4	Rib Right 6	0.929	8.8	0.822	13.0
Rib Left 7	0.921	8.3	0.854	12.9	Rib Right 7	0.931	9.4	0.874	17.8
Rib Left 8	0.914	8.3	0.742	99.5	Rib Right 8	0.927	8.3	0.843	20.6
Rib Left 9	0.906	8.8	0.773	84.9	Rib Right 9	0.925	7.6	0.848	46.4
Rib Left 10	0.921	6.4	0.828	48.1	Rib Right 10	0.937	7.2	0.865	35.9
Rib Left 11	0.915	5.9	0.904	7.8	Rib Right 11	0.940	4.1	0.898	8.2
Rib Left 12	0.881	17.1	0.882	5.1	Rib Right 12	0.899	7.9	0.857	5.3

The complete framework (**CAR + Aug**) consistently surpasses the strong Full Aug baseline across all categories. Most notably, CAR addresses the topological ambiguity in the challenging lateral projection, driving a substantial +1.51% DSC improvement in the Lateral Rib group and a +0.57% boost in the Lateral Lung group. This specific enhancement confirms that CAR effectively regularizes shape constraints in highly superimposed regions where standard data augmentation plateaus.

3.3. Downstream Clinical Utility

We demonstrate the functional value of our segmentations by visualizing their utility across two proposed downstream clinical tasks and quantifying their performance in disease classification.

Cardiothoracic Ratio (CTR) Demonstration: We demonstrate the utility of our cardiac segmentation by visually illustrating the CTR measurement in Fig. 9. The figure shows the accurate delineation of the heart and the measurement lines used to derive the ratio between the maximal transverse cardiac di-

Table 2: Segmentation Statistics by Organ Group Following Expert Revision (PA and LA Views)

Group: PA	DSC↑	Std DSC	HD↓	Std HD	Group: LA	DSC↑	Std DSC	HD↓	Std HD
Heart & Vessels	0.926	0.068	43.8	23.5	Heart & Vessels	0.967	0.047	47.5	77.5
Lung Group	0.891	0.058	81.7	53.8	Lung Group	0.982	0.034	55.8	98.9
Rib Group	0.894	0.143	47.6	23.8	Rib Group	0.837	0.190	118.4	177.6
Vertebrae Group	0.943	0.154	8.1	18.8	Vertebrae Group	0.795	0.299	78.4	113.3
Other Bone Group	0.978	0.046	7.7	15.5	Other Bone Group	0.925	0.173	23.9	60.8

Table 3: Ablation Study of DSC for Major Views and Organ Sub-Groups

Organ Group	Plain↑	PostHoc↑	MSDR↑	Full Aug↑
PA View	91.62%	93.75%	94.03%	94.53%
Heart & Vessels	90.84%	93.05%	93.92%	93.30%
Lung	93.47%	94.27%	95.57%	95.30%
Rib	90.07%	93.38%	93.08%	93.65%
Vertebrae	90.21%	94.15%	94.64%	94.67%
Other Bone	93.53%	95.39%	95.85%	95.73%
LA View	85.98%	89.16%	87.60%	91.35%
Heart & Vessels	91.27%	92.27%	91.82%	92.23%
Lung	90.30%	92.81%	93.89%	93.89%
Rib	76.44%	80.94%	82.50%	86.24%
Vertebrae	89.39%	93.14%	93.03%	93.88%
Other Bone	82.49%	86.65%	86.19%	90.53%

Table 4: Segmentation-Guided Chest X-ray Disease Classification

Pathology	Raw CXR	CXR w/mask	Δ AUC	Improve %
Mean AUROC	80.26%	82.30%	2.04%	2.54%
Pleural Thickening	76.83%	80.13%	3.30%	4.30%
Atelectasis	81.09%	84.45%	3.36%	4.14%
Mass	86.46%	89.56%	3.10%	3.59%
Cardiomegaly	90.14%	93.33%	3.19%	3.54%
Effusion	87.45%	90.39%	2.94%	3.36%
Emphysema	86.66%	89.38%	2.72%	3.14%
Pneumothorax	86.83%	89.30%	2.47%	2.84%
Fibrosis	77.72%	79.82%	2.10%	2.70%
Pneumonia	67.94%	69.48%	1.54%	2.27%
Consolidation	77.28%	78.69%	1.41%	1.82%
Infiltration	63.80%	64.71%	0.91%	1.43%
Edema	79.37%	80.42%	1.05%	1.32%
Hernia	85.36%	85.75%	0.39%	0.46%
Nodule	76.64%	76.72%	0.08%	0.10%

ameter and the maximal transverse thoracic diameter. Quantitatively, the derived CTR scores achieved an AUC of 0.93 with a statistically significant separation ($p \ll 0.001$) between normal and cardiomegaly subjects.

Spine Curvature Assessment (SPCA) Validation: We validate the utility of our instance-level vertebral segmentation by visualizing its application to SPCA in Fig. 10. The accompanying figure demonstrates the model’s ability to precisely identify and track the thoracic vertebral centroids. This measure allows for a preliminary, automated stratification of cases into one of three urgency levels, indicating the need for further clinical evaluation or immediate attention. In our evaluation, this metric achieved an AUC of 0.87 with a statistically significant separation ($p \ll 0.001$), validating its effectiveness as a reliable screening tool for spinal deformities.

Segmentation-Guided Disease Classification: We report the AUC for the detection of all 14 diseases on the CXR14 dataset in Table 4. We compare the performance of the baseline raw CXR classifier against the Segmentation-Guided classifier. Quantitatively, the segmentation-guided model achieved a Mean AUROC of 82.30%, representing a 2.04% absolute increase over the 80.26% baseline. The most significant improvements were observed in Atelectasis (+3.36% AUC) and Pleural Thickening (+3.30% AUC), validating the role of explicit anatomical guidance in boosting diagnostic performance.

4. Discussion

In this work, we introduced AnyCXR, a unified framework that combines Multi-stage Domain Randomization (MSDR)

with Conditional Joint Annotation Regularization (CAR) to achieve robust, generalizable anatomy segmentation across arbitrary projection angles using only synthetic supervision. Our experiments demonstrate that the model effectively bridges the domain gap between synthetic and clinical radiographs. In PA views, AnyCXR achieves precise boundary adherence, while in lateral views it maintains strong volumetric recovery despite substantial anatomical overlap that typically complicates segmentation. These findings indicate that the MSDR engine successfully captures the breadth of visual and geometric variability encountered in real-world imaging. Clinical benchmarking further confirms the practical utility of the framework. As shown in Table 1, AnyCXR performs reliably as a pre-annotation tool and yields high agreement with expert labels across multiple anatomical structures. Ablation experiments in Table 3 highlight the role of CAR in improving topological consistency, particularly in regions where structures overlap or exhibit subtle boundaries. Beyond segmentation accuracy, AnyCXR also demonstrates value for downstream clinical tasks. The anatomically informed features support population-level screening workflows, achieving high accuracy for cardiothoracic ratio estimation and spine curvature assessment, and they provide explicit spatial priors that significantly enhance disease classification performance (Table 4). Taken together, these results suggest that AnyCXR offers a scalable and effective foundation for generalizable CXR analysis.

Although the framework demonstrates strong performance, several limitations remain, many of which stem from the synthetic data generation process. One limitation arises from the

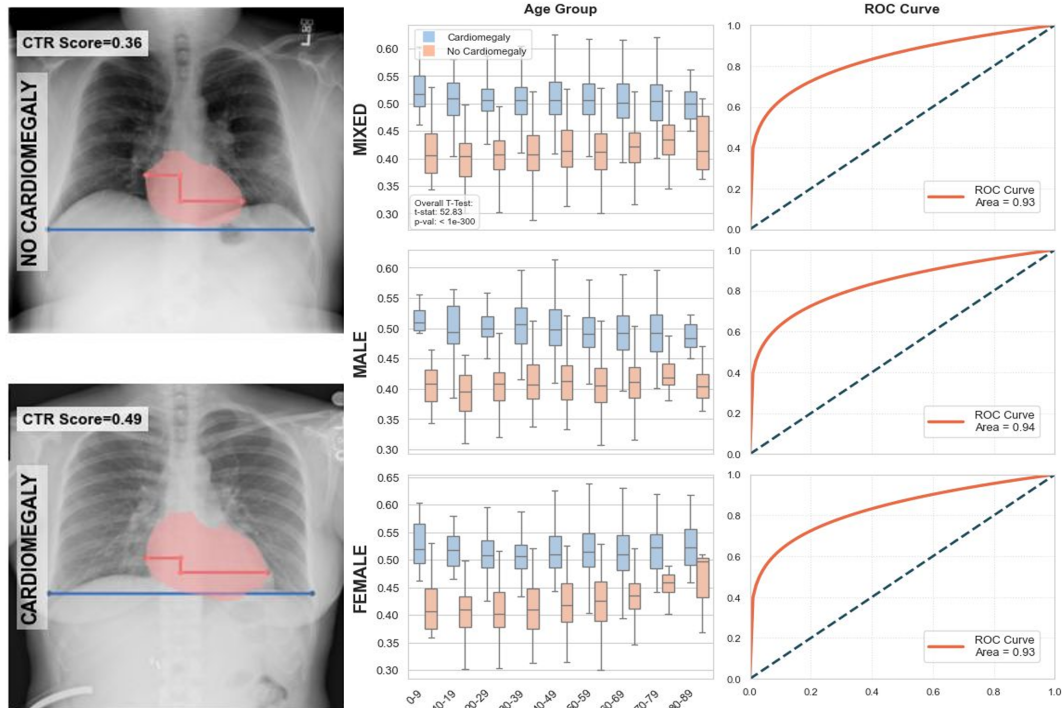


Figure 9: **Visualization for CTR disease detection:** This figure demonstrates the utility of the segmentation model for automatic Cardiothoracic Ratio (CTR) assessment in the PA view. The left panel shows the delineated heart and the measurement lines used to calculate the CTR score, distinguishing between a normal case and a pathological case. The right panels illustrate the ROC curves and distribution of derived CTR scores, achieving an overall AUC of 0.93 with statistically significant separation between normal and cardiomegaly subjects across age and gender groups.

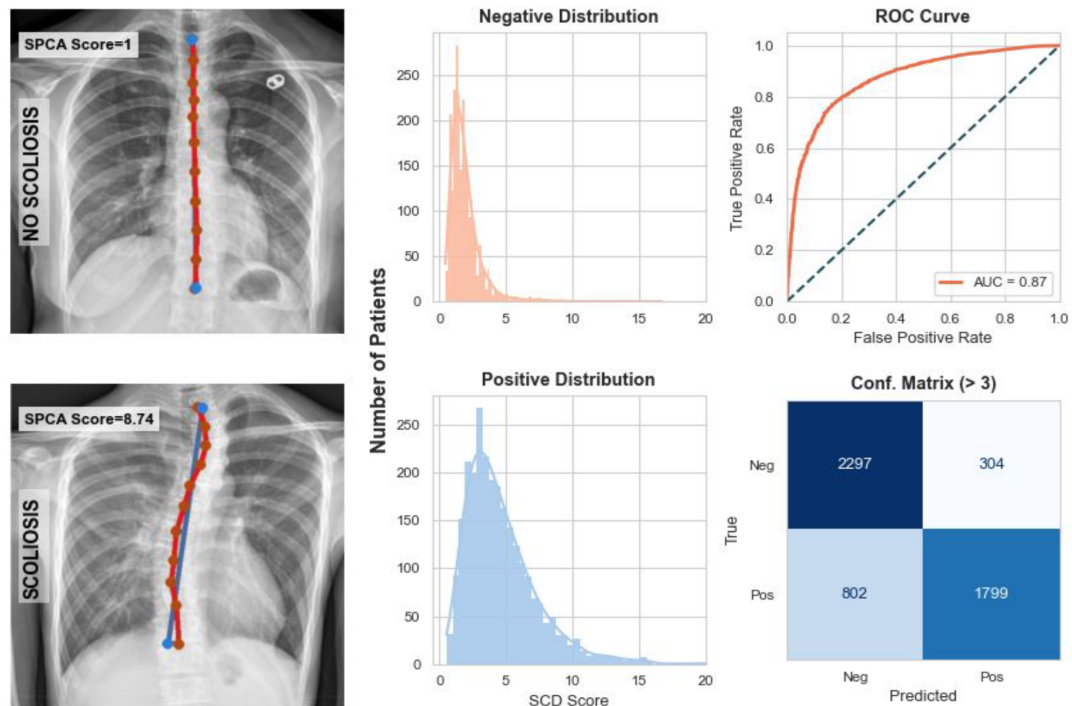


Figure 10: **Visualization for SPCA disease detection:** This figure demonstrates the clinical utility of instance-level vertebral segmentation for preliminary Spine Curvature Assessment (SPCA). The left panel illustrates the identification and tracking of thoracic vertebral centroids to measure deviation, distinguishing between a normal spine and a case with probable scoliosis. The center and right panels show the distribution of SPCA scores and the ROC curve, achieving an AUC of 0.87, which validates its effectiveness as a screening tool for spinal deformities.

automated 3D segmentation masks used as ground-truth labels for CT volumes. These masks occasionally contain voxel-level jaggedness or surface irregularities that become amplified when projected into 2D. Interestingly, the model, guided by the CAR regularizer, often produces smoother and more anatomically consistent boundaries than the synthetic labels themselves. This behavior is desirable from a clinical perspective, yet it can penalize overlap-based metrics on the synthetic test set and lead to lower DSC and higher HD values even when the predictions qualitatively appear superior. A second limitation relates to the divergence between anatomically correct projections derived from CT and the stylistic conventions of clinical 2D annotation. Radiologists typically delineate structures according to visible intensity transitions rather than their true anatomical extent. As a result, the model often predicts anatomically accurate boundaries that differ from the consensus appearance of standard radiographs, particularly for lung lobes and costovertebral junctions. Because AnyCXR is trained exclusively on DRR data, expert annotators frequently corrected these regions to align with clinical practice, which produced a measurable drop in performance when compared with human labels. For applications that prioritize conformity to 2D clinical conventions, fine-tuning the model with a small set of expert-annotated CXRs may help reconcile this semantic gap.

Additional limitations point to directions for future development. *First*, the current projection pipeline relies on DRR-based ray casting, which does not account for several physical effects present in real CXR, including scatter, beam hardening, detector blur, and anti-scatter grid interactions. DRR rendering was chosen primarily for computational efficiency, enabling large-scale data generation within practical time and hardware constraints. As simulation tools and computing resources advance, incorporating more physically realistic projection models, including Monte Carlo or hybrid approaches, may allow AnyCXR to more closely approximate clinical imaging conditions and further enhance generalization. *Second*, the segmentation backbone within the CAR framework remains deliberately simple. We employed a UNet with residual blocks to isolate and evaluate the contributions of MSDR and CAR, yet even this lightweight model achieves strong cross-view performance. Since the segmentation module is fully interchangeable, future work will examine newer architectures such as transformer-based encoders and diffusion-based segmentation models, which may improve boundary precision and robustness in anatomically complex regions. *Third*, AnyCXR is trained entirely on synthetic data. While the model exhibits excellent zero-shot generalization to clinical radiographs, synthetic-only training does not expose the network to the full spectrum of acquisition artifacts, disease-induced morphological changes, or scanner-specific variations encountered in practice. From another perspective, AnyCXR can be interpreted as an anatomy-focused foundation model for CXR, with strong structural recognition across diverse viewing geometries. A promising direction for future research involves using this model as an initialization for downstream tasks and exploring how limited real data can be used to adapt the model to specialized clinical applications.

5. Conclusion

We presented AnyCXR, a unified framework that enables comprehensive and generalizable anatomical segmentation for chest radiographs acquired at arbitrary angles. By integrating a large-scale Multi-stage Domain Randomization engine with the Conditional Joint Annotation Regularization framework, our method learns effectively from synthetic, partially labeled data and achieves strong zero-shot performance on real clinical images. The resulting anatomical maps consistently support downstream tasks, including cardiothoracic ratio estimation, spine curvature assessment, and disease classification, demonstrating the practical value of anatomically informed CXR analysis. Overall, AnyCXR offers a scalable foundation for future CXR-based AI systems, and continued advances in projection simulation and model architectures may further enhance its clinical applicability.

CRedit authorship contribution statement

Zifei Dong: Writing – original draft, Visualization, Validation, Software, Project administration, Methodology, Investigation, Conceptualization. **Wenjie Wu:** Data curation, Formal analysis, Resources. **Jinkui Hao:** Writing – review & editing. **Tianqi Chen:** Data Collection, Visualization. **Ziqiao Weng:** Writing – review & editing. **Bo Zhou:** Writing – review & editing, Supervision, Project administration, Methodology, Investigation, Conceptualization.

Declaration of competing interest

The authors declare that they have no known competing financial interests or personal relationships that could have appeared to influence the work reported in this paper.

References

- Akhter, Y., Singh, R., Vatsa, M., 2023. Ai-based radiodiagnosis using chest x-rays: A review. *Frontiers in Big Data* 6. URL: <https://www.frontiersin.org/journals/big-data/articles/10.3389/fdata.2023.1120989/full>, doi:10.3389/fdata.2023.1120989. accessed: 2025.
- Akinci D'Antonoli, T., Berger, L.K., Indrakanti, A.K., Vishwanathan, N., Weiss, J., Jung, M., Berkarda, Z., Rau, A., Reisert, M., Küstner, T., et al., 2025. Totalsegmentator mri: Robust sequence-independent segmentation of multiple anatomic structures in mri. *Radiology* 314, e241613.
- Azimi, H., Zhang, J., Xi, P., Asad, H., Ebadi, A., Tremblay, S., Wong, A., 2022. Improving classification model performance on chest x-rays through lung segmentation. *arXiv preprint arXiv:2202.10971* doi:10.48550/arXiv.2202.10971, arXiv:2202.10971.
- Calli, E., Sogancioglu, E., van Ginneken, B., van Leeuwen, K.G., Murphy, K., 2021. Deep learning for chest x-ray analysis: A survey. *Medical Image Analysis* 72, 102125. doi:10.1016/j.media.2021.102125.
- Candemir, S., Antani, S., 2019. A review on lung boundary detection in chest x-rays. *International Journal of Computer Assisted Radiology and Surgery* 14, 563–576. doi:10.1007/s11548-019-01917-1.
- Deng, J., Dong, W., Socher, R., Li, L.J., Li, K., Fei-Fei, L., 2009. Imagenet: A large-scale hierarchical image database, in: 2009 IEEE Conference on Computer Vision and Pattern Recognition, IEEE. pp. 248–255. doi:10.1109/CVPR.2009.5206848.

- Dey, N., Abulnaga, S.M., Billot, B., Abaci Turk, E., Grant, P.E., Dalca, A.V., Golland, P., 2023. Anystar: Domain randomized universal star-convex 3d instance segmentation. URL: <https://arxiv.org/abs/2307.07044v1>, doi:10.48550/arXiv.2307.07044, arXiv:2307.07044. submitted on 13 Jul 2023; Code available at <https://github.com/abulnaga/Anystar>; Subjects: Computer Vision and Pattern Recognition (cs.CV); Machine Learning (cs.LG).
- Dey, N., Billot, B., Wong, H.E., Wang, C.J., Ren, M., Grant, P.E., Dalca, A.V., Golland, P., 2024. Learning general-purpose biomedical volume representations using randomized synthesis. arXiv preprint arXiv:2411.02372v2 URL: <https://arxiv.org/abs/2411.02372v2>, doi:10.48550/arXiv.2411.02372. ICLR 2025 (International Conference on Learning Representations); Code & model weights available; Keywords: synthetic data, representation learning, medical image analysis, image registration, image segmentation.
- Gaggion, N., Mosquera, C., Mansilla, L., Saidman, J.M., Aineseder, M., Milone, D.H., Ferrante, E., 2024. Chexmask: a large-scale dataset of anatomical segmentation masks for multi-center chest x-ray images. Scientific Data 11, 511. URL: <https://www.nature.com/articles/s41597-024-03358-1>, doi:10.1038/s41597-024-03358-1.
- Gao, C., Killeen, B.D., Hu, Y., Grupp, R.B., Taylor, R.H., Armand, M., Unberath, M., 2023. Synthetic data accelerates the development of generalizable learning-based algorithms for x-ray image analysis. Nature Machine Intelligence 5, 294–308. doi:10.1038/s42256-023-00629-1.
- van Ginneken, B., Stegmann, M.B., Loog, M., 2006. Segmentation of anatomical structures in chest radiographs using supervised methods: a comparative study on a public database. Medical Image Analysis 10, 19–40. doi:10.1016/j.media.2005.02.002.
- Gopalakrishnan, V., Golland, P., 2023. Fast auto-differentiable digitally reconstructed radiographs for solving inverse problems in intraoperative imaging, in: Chen, Y., Linguraru, M.G., Shekhar, R., Wesarg, S., Erdt, M., Drechsler, K., Oyarzun Laura, C. (Eds.), Clinical Image-Based Procedures. CLIP 2022, Springer, Cham. pp. 1–11. doi:10.1007/978-3-031-23179-7_1.
- Gothi, R., 2025. Positioning in Chest X-Rays. Springer Nature Singapore, Singapore. pp. 11–19. URL: https://doi.org/10.1007/978-981-96-4816-0_2, doi:10.1007/978-981-96-4816-0_2.
- Gupte, T., Niljkar, M., Gawali, M., Kulkarni, V., Kharat, A., Pant, A., 2021. Deep learning models for calculation of cardiothoracic ratio from chest radiographs for assisted diagnosis of cardiomegaly. URL: <https://arxiv.org/abs/2101.07606>, arXiv:2101.07606.
- Hamamci, I.E., Er, S., Almas, F., Simsek, A.G., Esirgun, S.N., Dogan, I., Dasedelen, M.F., Durugol, O.F., Wittmann, B., Amiranashvili, T., Simsar, E., Simsar, M., Erdemir, E.B., Alanbay, A., Sekuboyina, A., Lafci, B., Bluethgen, C., Ozdemir, M.K., Menze, B., 2024. Developing generalist foundation models from a multimodal dataset for 3d computed tomography. URL: <https://arxiv.org/abs/2403.17834>, arXiv:2403.17834.
- Hanley, J.A., McNeil, B.J., 1982. The meaning and use of the area under a receiver operating characteristic (roc) curve. Radiology 143, 29–36. doi:10.1148/radiology.143.1.7063747.
- He, K., Zhang, X., Ren, S., Sun, J., 2016. Deep residual learning for image recognition, in: Proceedings of the IEEE Conference on Computer Vision and Pattern Recognition (CVPR), pp. 770–778.
- Hofmann, F.O., Heiliger, C., Tschaidse, T., Jarmusch, S., Auhage, L.A., Aghamaliyev, U., Gesenhues, A.B., Schiergens, T.S., Niess, H., Ilmer, M., Werner, J., Renz, B.W., 2025. Validation of body composition parameters extracted via deep learning-based segmentation from routine computed tomographies. Scientific Reports 15. URL: <https://www.nature.com/articles/s41598-025-55897-x>, doi:10.1038/s41598-025-55897-x.
- Hou, B., Zhu, Q., Mathai, T.S., Jin, Q., Lu, Z., Summers, R.M., 2024. Shadow and light: Digitally reconstructed radiographs for disease classification. URL: <https://arxiv.org/abs/2406.03688>, arXiv:2406.03688. submitted on 6 Jun 2024.
- Irvine, J., Rajpurkar, P., Ko, M., Yu, Y., Ciurea-Ilcus, S., Chute, C., Marklund, H., Haghighi, B., Ball, R., Shpanskaya, K., et al., 2019. Chexpert: a large chest radiograph dataset with uncertainty labels and expert comparison, in: Proceedings of the Thirty-Third AAAI Conference on Artificial Intelligence and Thirty-First Innovative Applications of Artificial Intelligence Conference and Ninth AAAI Symposium on Educational Advances in Artificial Intelligence (AAAI/IAAI/EAAI), AAAI Press. pp. 590–597. doi:10.1609/aaai.v33i01.3301590.
- Isensee, F., Jaeger, P.F., Kohl, S.A., Petersen, J., Maier-Hein, K.H., 2021. nnu-net: Self-adapting framework for u-net-based medical image segmentation. Nature Methods 18, 203–211. URL: <https://doi.org/10.1038/s41592-020-01008-z>, doi:10.1038/s41592-020-01008-z.
- Jaeger, S., Candemir, S., Antani, S., Wang, Y.X.J., Lu, P.X., Thoma, G., 2014. Two public chest x-ray datasets for computer-aided screening of pulmonary diseases. Quantitative Imaging in Medicine and Surgery 4, 475–477. doi:10.3978/j.issn.2223-4292.2014.11.20.
- Johnson, A.E.W., Pollard, T.J., Berkowitz, S.J., Greenbaum, N.R., Lungren, M.P., Deng, C.y., Mark, R.G., Horng, S., 2019. MIMIC-CXR, a de-identified publicly available database of chest radiographs with free-text reports. Scientific Data 6, 317. doi:10.1038/s41597-019-0322-0.
- Jones, C.M., Buchlak, Q.D., Oakden-Rayner, L., Milne, M., Seah, J., Esmaili, N., Hachey, B., 2021. Chest radiographs and machine learning - past, present and future. Journal of Medical Imaging and Radiation Oncology 65, 538–544. doi:10.1111/1754-9485.13274. epub 2021 Jun 25; Free access via PMC (PMC8453538).
- Kingma, D.P., Ba, J., 2015. Adam: A method for stochastic optimization, in: International Conference on Learning Representations (ICLR). doi:10.48550/arXiv.1412.6980. published as a conference paper at the 3rd International Conference for Learning Representations, San Diego, 2015.
- Lenga, M., Klinder, T., Bürger, C., von Berg, J., Franz, A., Lorenz, C., 2019. Deep learning based rib centerline extraction and labeling, in: Computational Methods and Clinical Applications in Musculoskeletal Imaging (MSKI 2018), Springer International Publishing. pp. 83–92. doi:10.1007/978-3-030-11166-3_9, arXiv:1809.07082.
- Maeda, Y., Nagura, T., Nakamura, M., Watanabe, K., 2023. Automatic measurement of the Cobb angle for adolescent idiopathic scoliosis using convolutional neural network. Scientific Reports 13, 14576. URL: <https://www.nature.com/articles/s41598-023-41821-y>, doi:10.1038/s41598-023-41821-y.
- Qin, C., Yao, D., Shi, Y., Song, Z., 2018. Computer-aided detection in chest radiography based on artificial intelligence: A survey. BioMedical Engineering Online 17. URL: <https://biomedical-engineering-online.biomedcentral.com/articles/10.1186/s12938-018-0544-y>, doi:10.1186/s12938-018-0544-y. open access; License: CC BY 4.0; Authors affiliated with Fudan University.
- Qureshi, I., Yan, J., Abbas, Q., Shaheed, K., Riaz, A.B., Wahid, A., Khan, M.W.J., Szczuko, P., 2023. Medical image segmentation using deep semantic-based methods: A review of techniques, applications and emerging trends. Information Fusion 90, 316–352.
- Ronneberger, O., Fischer, P., Brox, T., 2015. U-net: Convolutional networks for biomedical image segmentation, in: Navab, N., Hornegger, J., Wells, W.M., Frangi, A.F. (Eds.), Medical Image Computing and Computer-Assisted Intervention – MICCAI 2015, Springer, Cham. pp. 234–241. doi:10.1007/978-3-319-24574-4_28.
- Sebro, R., Mongan, J., 2023. TotalSegmentator: A gift to the biomedical imaging community. Radiology: Artificial Intelligence 5. URL: <https://doi.org/10.1148/ryai.230235>, doi:10.1148/ryai.230235. free access; Commentary; See related article: TotalSegmentator.
- Seibold, C., Jaus, A., Fink, M.A., Kim, M., Reiß, S., Herrmann, K., Kleesiek, J., Stiefelhagen, R., 2023. Accurate fine-grained segmentation of human anatomy in radiographs via volumetric pseudo-labeling. arXiv preprint arXiv:2306.03934 doi:10.48550/arXiv.2306.03934, arXiv:2306.03934.
- Seibold, C., Reiss, S., Sarfraz, S., Fink, M.A., Mayer, V., Sellner, J., Kim, M.S., Maier-Hein, K.H., Kleesiek, J., Stiefelhagen, R., 2022. Detailed annotations of chest x-rays via ct projection for report understanding, in: Proceedings of the 33rd British Machine Vision Conference (BMVC). doi:10.48550/arXiv.2210.03416.
- Sharma, V., Prakash, Verma, K., Vashishth, T.K., Kumar, B., Chaudhary, S., 2024. A unified deep learning approach for lung segmentation in x-ray images, in: 2024 International Conference on Electronics, Computing, Communication and Control Technology (ICECCC), IEEE. pp. 1–6. doi:10.1109/ICECCC61767.2024.10593950.
- Tajbakhsh, N., Jeyaseelan, L., Li, Q., Chiang, J.N., Wu, Z., Ding, X., 2020. Embracing imperfect datasets: A review of deep learning solutions for medical image segmentation. Medical Image Analysis 63, 101693. doi:10.1016/j.media.2020.101693.
- Wang, H., Zhang, D., Feng, J., Cascone, L., Nappi, M., Wan, S., 2024. A multi-objective segmentation method for chest x-rays based on collaborative learning from multiple partially annotated datasets. Information Fusion 102, 102016. doi:10.1016/j.inffus.2023.102016.
- Wang, X., Peng, Y., Lu, L., Lu, Z., Bagheri, M., Summers, R.M., 2017. Chestx-

- ray8: Hospital-scale chest x-ray database and benchmarks on weakly-supervised classification and localization of common thorax diseases, in: Proceedings of the IEEE Conference on Computer Vision and Pattern Recognition (CVPR), pp. 2097–2106. doi:10.1109/CVPR.2017.369.
- Wasserthal, J., Breit, H.C., Meyer, M.T., Pradella, M., Hinck, D., Sauter, A.W., Heye, T., Boll, D.T., Cyriac, J., Yang, S., Bach, M., Segeroth, M., 2023. Totalsegmentator: Robust segmentation of 104 anatomic structures in ct images. *Radiology: Artificial Intelligence* 5, e230024. doi:10.1148/ryai.230024.
- Xue, P., Niu, S., 2024. A novel active contour model based on features for image segmentation. *Pattern Recognition* 155, 110673. doi:10.1016/j.patcog.2024.110673.
- Yi, L., Zhang, L., Zhao, K., Xu, X., 2025. Learning from certain regions of interest in medical images via probabilistic positive-unlabeled networks. *Medical Image Analysis* 88, 103745. URL: <https://pubmed.ncbi.nlm.nih.gov/40779832/>, doi:10.1016/j.media.2025.103745.

Appendix A. MSDR Implementation Details

In this section, we detail the mathematical formulations and hyperparameters used in the MSDR engine. The pipeline consists of 3D pre-projection augmentations followed by 2D post-projection detector simulations. We apply the following augmentations, each with uniform probability to individual masks.

Notation and Mask Definitions

We define the volumetric segmentation masks used to isolate specific anatomical structures for targeted augmentation. Let $\Omega \subset \mathbb{R}^3$ denote the spatial domain of the CT volume. We define the set of all anatomical masks as $\mathcal{M}_{\text{ROI}} = M_s \cup M_b$, where:

- **Soft Tissue (M_s):** The combined mask for all soft tissue structures.
- **Bone (M_b):** The global mask for all osseous structures.

It is explicitly noted that augmentations are restricted to voxels $x \in \mathcal{M}_{\text{ROI}}$. Voxels belonging to the background (air) or unmasked regions, $x \in \Omega \setminus \mathcal{M}_{\text{ROI}}$, remain invariant throughout the 3D augmentation pipeline.

Additionally, we define specific subsets of the bone mask:

- **Vertebrae:** $\mathcal{V} = \{V_{T2}, V_{T3}, \dots, V_{T12}\}$.
- **Ribs:** $\mathcal{R}_L = \{R_{L1}, \dots, R_{L12}\}$ and $\mathcal{R}_R = \{R_{R1}, \dots, R_{R12}\}$.

3D Attenuation Augmentations

Here, we detail the volumetric operations applied to modify the Hounsfield Units (HU) of the anatomical structures prior to the generation of the DRR.

Bone-to-soft-tissue attenuation randomization This augmentation is applied with probability $p = 0.4$. We apply anti-correlated scaling factors to M_s and M_b to disrupt consistent contrast relationships. We define two range intervals: $S_{\text{high}} = [1.0, 1.7]$ and $S_{\text{low}} = [0.3, 1.0]$ and we randomly assign a tissue type $T_1 \in \{M_s, M_b\}$ to sample from S_{high} and the other T_2 to sample from S_{low} . Let $s_1 \sim \mathcal{U}(S_{\text{high}})$ and $s_2 \sim \mathcal{U}(S_{\text{low}})$.

The voxel intensities $H(x)$ are updated as:

$$H'(x) = \begin{cases} H(x) \cdot s_1 & \text{if } x \in T_1 \\ H(x) \cdot s_2 & \text{if } x \in T_2 \end{cases} \quad (\text{A.1})$$

Inter-bone attenuation randomization We introduce two augmentation strategies to enhance bone density heterogeneity. The first decouples intensity correlations between adjacent bone structures, while the second simulates longitudinal attenuation gradients caused by varying tissue thickness and anatomical positioning.

- **Random Component Scaling:** We apply HU value scaling for individual bone components, $\mathcal{K} = \mathcal{V} \cup \mathcal{R}_L \cup \mathcal{R}_R$ with probability $p = 0.3$. For each distinct bone mask $M_k \in \mathcal{K}$, a unique scaling factor $s_k \sim \mathcal{U}(0.3, 1.7)$ is sampled. The intensity for voxels belonging to that specific bone is updated as:

$$H'(x) = H(x) \cdot s_k, \quad \forall x \in M_k \quad (\text{A.2})$$

- **Vertical Gradient Scale:** We apply HU scaling along the vertical Z-axis (head-to-foot) to the spine ($\cup \mathcal{V}$), left ribs ($\cup \mathcal{R}_L$), and right ribs ($\cup \mathcal{R}_R$) independently with $p = 0.4$. For each group, a normalized coordinate $\hat{z} \in [0, 1]$ spans the region from superior ($\hat{z} = 0$) to inferior ($\hat{z} = 1$). We sample $S_{\text{head}} \in [0.9, 1.5]$, $S_{\text{foot}} \in [0.6, 0.9]$, and $\alpha \in [0.5, 1.5]$ to define the scaling factor:

$$S(\hat{z}) = S_{\text{foot}} + (1 - \hat{z})^\alpha \cdot (S_{\text{head}} - S_{\text{foot}}) \quad (\text{A.3})$$

This factor is applied uniformly to all bone voxels within a given slice z .

Intra-bone attenuation randomization We apply a morphology-based gradient to enhance the variation for the density transition from the cortical surface to the trabecular core with probability $p = 0.7$. We define depth via iterative erosion to handle irregular bone shapes.

Let $\delta(x) \in [0, 1]$ denote the normalized morphological depth of voxel x , where $\delta = 0$ corresponds to the outer surface and $\delta = 1$ to the deepest core layer found by recursive binary erosion. We sample surface and core scaling factors $S_{\text{surf}} \sim \mathcal{U}(0.9, 1.5)$ and $S_{\text{core}} \sim \mathcal{U}(0.6, 1.1)$. The intensity update is defined as:

$$H'(x) = H(x) \cdot [S_{\text{surf}} + \delta(x)^\alpha \cdot (S_{\text{core}} - S_{\text{surf}})] \quad (\text{A.4})$$

where $\alpha \in [0.5, 1.5]$ controls the gradient curvature.

Soft-tissue attenuation randomization We apply one of two mutually exclusive augmentations to M_s .

- **Standard Scaling ($p = 0.6$):** We apply a uniform scalar $s \sim \mathcal{U}(0.3, 1.7)$ to each soft tissue voxel in M_s : $H'(x) = H(x) \cdot s$.
- **Polarity Inversion ($p = 0.3$):** To simulate extreme contrast reversal, we map soft tissue values to a positive range. We sample a drift $\delta \sim \mathcal{U}(-0.1, 0.1)$ and apply the transformation:

$$H'(x) = -(1.5 + \delta) \cdot H(x) \quad (\text{A.5})$$

This is applied to voxels within the valid soft tissue range (e.g., $HU \in [-900, -2]$).

Geometric and Noise Augmentations

This section outlines the stochastic perturbations applied to the projection geometry parameters, as well as the injection of noise and synthetic foreign objects into the simulation environment.

Noise and artifacts

- **Gaussian Noise ($p = 0.3$):** Voxel-wise additive noise $N \sim \mathcal{N}(0, \sigma^2)$ is added to the volume, where σ is uniformly sampled per volume from $[10, 50]$ HU.
- **External Objects ($p = 0.2$):** We inject $N \in \{1, 2, 3\}$ synthetic objects (cylinders or ellipsoids). Dimensions are sampled uniformly (Radius $\sim \mathcal{U}(5, 20)$ mm, Length $\sim \mathcal{U}(10, 60)$ mm) and objects are assigned $HU \in (1800, 2000)$ to simulate dense foreign bodies.

Projection geometry randomization

- **Source-to-Detector distance (SDD):** Applied with $p = 0.4$. The SDD is perturbed by a factor $s_{sod} \sim \mathcal{U}(0.9, 1.1)$.
- **Object-to-Detector Distance (ODD):** Applied with $p = 0.4$. A vertical offset $\Delta h \sim \mathcal{U}(-30, 30)$ mm is added to the ODD.

2D Post-Projection Augmentations

Finally, we describe the image-level transformations applied to the projected 2D radiographs to simulate varying detector responses and exposure conditions.

Exposure and Detector-response Normalization With probability $p = 0.7$, we apply a piecewise-linear tone mapping defined by a randomized control point (x'_c, y'_c) . We sample the knot coordinates as $x'_c \sim \mathcal{U}[-0.2, 0.4]$ and $y'_c \sim \mathcal{U}[-0.2, 0.4]$. The final pixel intensity is obtained by linear interpolation between the anchors $(0, 0)$, (x'_c, y'_c) , and $(1, 1)$.

Polarity perturbation With probability $p = 0.3$, we invert the global intensity of the 2D image I :

$$I_{\text{new}} = (I_{\min} + I_{\max}) - I + \epsilon \quad (\text{A.6})$$

where ϵ is a small stability term.

Appendix B. Model Implementation Details

The segmentation backbone is constructed as a U-Net with a ResNet-50 encoder. We initialize the network using a standard ImageNet-pretrained ResNet-50 and adapt the first convolutional block (`conv1`) to handle the single-channel CXR inputs. The encoder stages expose the feature maps after `conv1 + bn1 + relu + maxpool` and `layer1` through `layer4`, yielding feature strides of $1/4$, $1/8$, $1/16$, and $1/32$ of the input resolution. Input CXR images are normalized to the range $[0, 1]$ prior to processing. The decoder mirrors these scales, using transposed convolutions and skip connections at each up-sampling stage to reconstruct the final multi-class probability maps.

The CAR framework operates on the full multi-class probability maps without downsampling. The CAR encoder G_{θ_1} is conditioned by using direct channel-wise concatenation of the input image \mathbf{X} and the prediction $\hat{\mathbf{Y}}$. The encoder consists of two convolutional blocks: a 3×3 convolution mapping from $C_{\text{in}}^{\text{CAR}}$ channels (where $C_{\text{in}}^{\text{CAR}}$ is 1 plus the number of output classes) to $C_{\text{lat}}/4$ channels, followed by batch normalization, ReLU, and a single 4×4 max-pooling layer (resulting in overall $4\times$ spatial downsampling), and a second 3×3 convolution to C_{lat} channels with batch normalization and ReLU. The CAR decoder G_{θ_2} is a lightweight symmetric stack comprising two 4×4 transposed convolutions (stride 2, padding 1) that upsample from C_{lat} to $C_{\text{lat}}/2$ and then to $C_{\text{lat}}/4$, each followed by batch normalization and ReLU, and a final 1×1 convolution to the output channel dimension with sigmoid activation.

Appendix C. Detailed Distribution of Labels

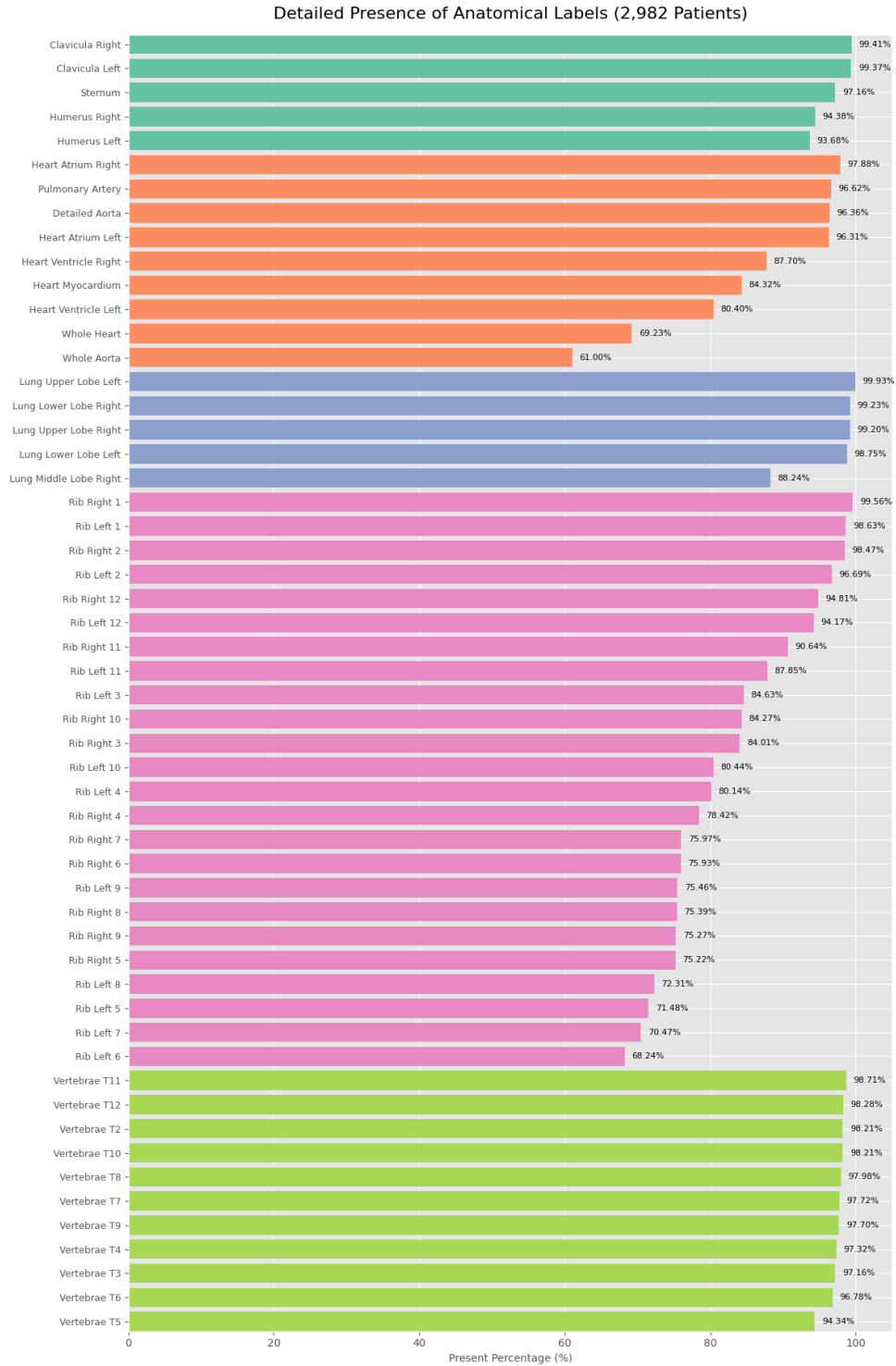


Figure C.11: Detailed distribution of each organ after filtering

Appendix D. Segmentation Comparison of DRR Images in Oblique View

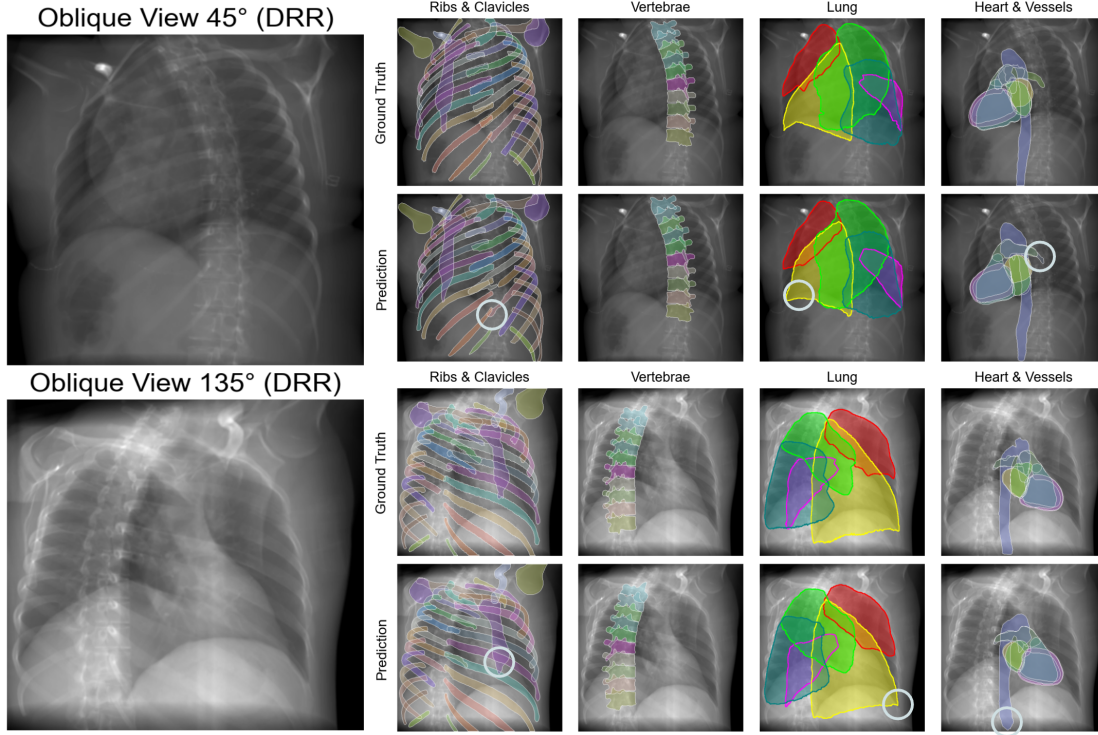


Figure D.12: Segmentation Comparison on Synthetic Oblique View DRRs

Appendix E. Segmentation Performance of Oblique View

Table E.5: Dice and Hausdorff Distance (pixels) by Anatomical Structure for the Oblique View

Structure	45° DSC↑	45° HD↓	135° DSC↑	135° HD↓	Structure	45° DSC↑	45° HD↓	135° DSC↑	135° HD↓
Vertebra T2	0.913	5.8	0.909	10.5	Whole Heart	0.905	27.5	0.921	28.2
Vertebra T3	0.916	6.1	0.926	7.4	Heart Atrium Left	0.838	14.1	0.890	11.3
Vertebra T4	0.936	5.4	0.919	7.5	Heart Atrium Right	0.825	19.2	0.894	13.5
Vertebra T5	0.942	5.3	0.921	7.2	Heart Myocardium	0.940	8.4	0.931	11.6
Vertebra T6	0.929	9.3	0.932	7.6	Heart Ventricle Left	0.926	10.2	0.921	10.2
Vertebra T7	0.933	3.3	0.940	5.8	Heart Ventricle Right	0.869	20.4	0.917	12.6
Vertebra T8	0.932	4.4	0.939	4.9	Pulmonary Artery	0.866	18.9	0.890	15.1
Vertebra T9	0.912	10.8	0.944	6.6	Aorta	0.898	13.2	0.885	26.2
Vertebra T10	0.923	8.4	0.939	7.5	Lung	0.925	23.3	0.935	25.9
Vertebra T11	0.938	5.0	0.935	6.8	Lung Upper Lobe Left	0.928	26.8	0.932	24.7
Vertebra T12	0.932	7.5	0.938	7.3	Lung Lower Lobe Left	0.924	26.1	0.944	20.7
Clavicle Left	0.923	13.5	0.928	8.3	Lung Upper Lobe Right	0.947	17.6	0.939	22.3
Clavicle Right	0.929	3.8	0.938	5.2	Lung Middle Lobe Right	0.888	25.9	0.897	23.7
Humerus Left	0.961	5.3	0.875	8.1	Lung Lower Lobe Right	0.925	24.8	0.928	31.1
Humerus Right	0.963	3.4	0.959	6.8	Sternum	0.905	21.3	0.917	15.2
Rib Left 1	0.918	6.0	0.899	11.8	Rib Right 1	0.910	5.2	0.906	7.1
Rib Left 2	0.900	7.0	0.871	15.0	Rib Right 2	0.880	8.1	0.902	11.2
Rib Left 3	0.877	11.8	0.838	32.5	Rib Right 3	0.919	5.8	0.911	7.2
Rib Left 4	0.907	9.3	0.838	26.4	Rib Right 4	0.911	9.4	0.920	7.1
Rib Left 5	0.886	19.0	0.865	23.3	Rib Right 5	0.910	18.2	0.926	8.5
Rib Left 6	0.847	25.3	0.879	17.8	Rib Right 6	0.882	30.0	0.932	6.6
Rib Left 7	0.900	18.3	0.903	13.7	Rib Right 7	0.913	17.2	0.934	7.6
Rib Left 8	0.923	18.3	0.885	17.7	Rib Right 8	0.916	12.1	0.914	11.7
Rib Left 9	0.933	9.7	0.889	18.6	Rib Right 9	0.918	6.4	0.909	15.2
Rib Left 10	0.821	28.9	0.918	13.2	Rib Right 10	0.893	26.3	0.923	16.8
Rib Left 11	0.768	30.0	0.932	5.8	Rib Right 11	0.835	31.3	0.922	6.8
Rib Left 12	0.835	18.3	0.912	6.2	Rib Right 12	0.911	3.4	0.887	6.7

Appendix F. Ablation Study of HD for LA and PA Views

Table F.6: Ablation Study of Hausdorff Distance (HD) in Pixels for Major Views and Organ Sub-Groups

Organ Group	Plain	PostHoc	MSDR	Full Aug
PA View	14.70	9.21	9.24	9.43
Heart & Vessels	14.81	11.11	9.68	9.84
Lung	23.84	20.44	16.68	18.03
Rib	13.78	7.94	9.56	7.65
Vertebrae	10.34	6.41	6.38	5.96
Other Bone	10.72	6.76	5.76	5.66
LA View	21.92	19.08	18.98	14.57
Heart & Vessels	14.14	12.62	17.33	13.75
Lung	30.37	27.47	23.90	23.20
Rib	33.79	29.58	24.35	18.59
Vertebrae	7.84	6.41	8.70	6.72
Other Bone	20.12	17.89	13.88	10.58